Stem Cell Reports
Article

ISSCR

OPEN ACCESS

Cardiomyocytes recruit monocytes upon SARS-CoV-2 infection by secreting CCL2

Liuliu Yang,[1,10] Benjamin E. Nilsson-Payant,[2,10] Yuling Han,[1,10] Fabrice Jaffré,[1,10] Jiajun Zhu,[1,10] Pengfei Wang,[3] Tuo Zhang,[4] David Redmond,[5] Sean Houghton,[5] Rasmus Møller,[2,9] Daisy Hoagland,[2,9] Lucia Carrau,[2] Shu Horiuchi,[2] Marisa Goff,[2] Jean K. Lim,[2] Yaron Bram,[6] Chanel Richardson,[6] Vasuretha Chandar,[6] Alain Borczuk,[7] Yaoxing Huang,[3] Jenny Xiang,[4] David D. Ho,[3,*] Robert E. Schwartz,[6,8,*] Benjamin R. tenOever,[2,*] Todd Evans,[1,*] and Shuibing Chen[1,*]

[1]Department of Surgery, Weill Cornell Medicine, 1300 York Avenue, New York, NY 10065, USA
[2]Department of Microbiology, Icahn School of Medicine at Mount Sinai, 1468 Madison Avenue, New York, NY 10029, USA
[3]Aaron Diamond AIDS Research Center, Columbia University Irving Medical Center, New York, NY 10032, USA
[4]Genomics Resources Core Facility, Weill Cornell Medicine, New York, NY 10065, USA
[5]Division of Regenerative Medicine, Ansary Stem Cell Institute, Weill Cornell Medicine, New York, NY 10065, USA
[6]Division of Gastroenterology and Hepatology, Department of Medicine, Weill Cornell Medicine, 1300 York Avenue, New York, NY 10065, USA
[7]Department of Pathology and Laboratory Medicine, Weill Cornell Medical College, New York, NY 10065, USA
[8]Department of Physiology, Biophysics and Systems Biology, Weill Cornell Medicine, 1300 York Avenue, New York, NY 10065, USA
[9]Graduate School of Biomedical Sciences, Icahn School of Medicine at Mount Sinai, 1468 Madison Avenue, New York, NY 10029, USA
[10]These authors contributed equally
*Correspondence: dh2994@cumc.columbia.edu (D.D.H.), res2025@med.cornell.edu (R.E.S.), benjamin.tenoever@mssm.edu (B.R.t.), tre2003@med.cornell.edu (T.E.), shc2034@med.cornell.edu (S.C.)
https://doi.org/10.1016/j.stemcr.2021.07.012

SUMMARY

Heart injury has been reported in up to 20% of COVID-19 patients, yet the cause of myocardial histopathology remains unknown. Here, using an established *in vivo* hamster model, we demonstrate that SARS-CoV-2 can be detected in cardiomyocytes of infected animals. Furthermore, we found damaged cardiomyocytes in hamsters and COVID-19 autopsy samples. To explore the mechanism, we show that both human pluripotent stem cell-derived cardiomyocytes (hPSC-derived CMs) and adult cardiomyocytes (CMs) can be productively infected by SARS-CoV-2, leading to secretion of the monocyte chemoattractant cytokine CCL2 and subsequent monocyte recruitment. Increased CCL2 expression and monocyte infiltration was also observed in the hearts of infected hamsters. Although infected CMs suffer damage, we find that the presence of macrophages significantly reduces SARS-CoV-2-infected CMs. Overall, our study provides direct evidence that SARS-CoV-2 infects CMs *in vivo* and suggests a mechanism of immune cell infiltration and histopathology in heart tissues of COVID-19 patients.

INTRODUCTION

The ongoing coronavirus disease 2019 (COVID-19) pandemic is caused by the betacoronavirus severe acute respiratory syndrome coronavirus 2 (SARS-CoV-2). While respiratory failure is a predominant outcome, cardiac involvement is a common feature in hospitalized COVID-19 patients and is associated with poor prognosis. For example, in a Wuhan cohort, 7% of total patients and 22% of critically ill patients suffered myocardial injury, demonstrated by elevated cardiac biomarkers, such as high-sensitivity troponin I (hs-cTnI), or by electrocardiography and echocardiogram abnormalities (Wang et al., 2020). hs-cTnI was reported to be above the 99th percentile upper reference in 46% of non-survivors as opposed to 1% of survivors (Zhou et al., 2020). The mortality risk associated with acute cardiac injury was more significant than age, chronic pulmonary disease, or prior history of cardiovascular disease (Guo et al., 2020; Shi et al., 2020). As emerging cases of COVID-19-related Kawasaki disease-like symptoms are reported, many children with COVID-19 also suffer from cardiac dysfunction (Riphagen et al., 2020). There are also case reports of myocarditis in COVID-19 patients (Gnecchi et al., 2020; Inciardi et al., 2020; Tavazzi et al., 2020). The cause of these cardiac injuries observed in COVID-19 patients is not yet established but could potentially involve increased cardiac stress due to respiratory failure and hypoxemia, direct myocardial infection by SARS-CoV-2, or indirect cardiotoxicity from a systemic inflammatory response.

We and other groups have reported SARS-CoV-2 infection in human pluripotent stem cell-derived cardiomyocytes (hPSC-derived CMs) *in vitro* (Bojkova et al., 2020; Sharma et al., 2020; Yang et al., 2020). SARS-CoV-2 infection might also cause damage of CMs (Marchiano et al., 2021). Although several studies have detected SARS-CoV-2 RNA in autopsy samples from hearts of COVID-19 patients (Escher et al., 2020; Lindner et al., 2020), the presence of SARS-CoV-2 in CMs remains controversial. Tavazzi et al. (2020) and Lindner et al. (2020) identified SARS-CoV-2 virions in the interstitial cells of the myocardium of COVID-19 patients. Furthermore, Dolhnikoff et al. (2020)

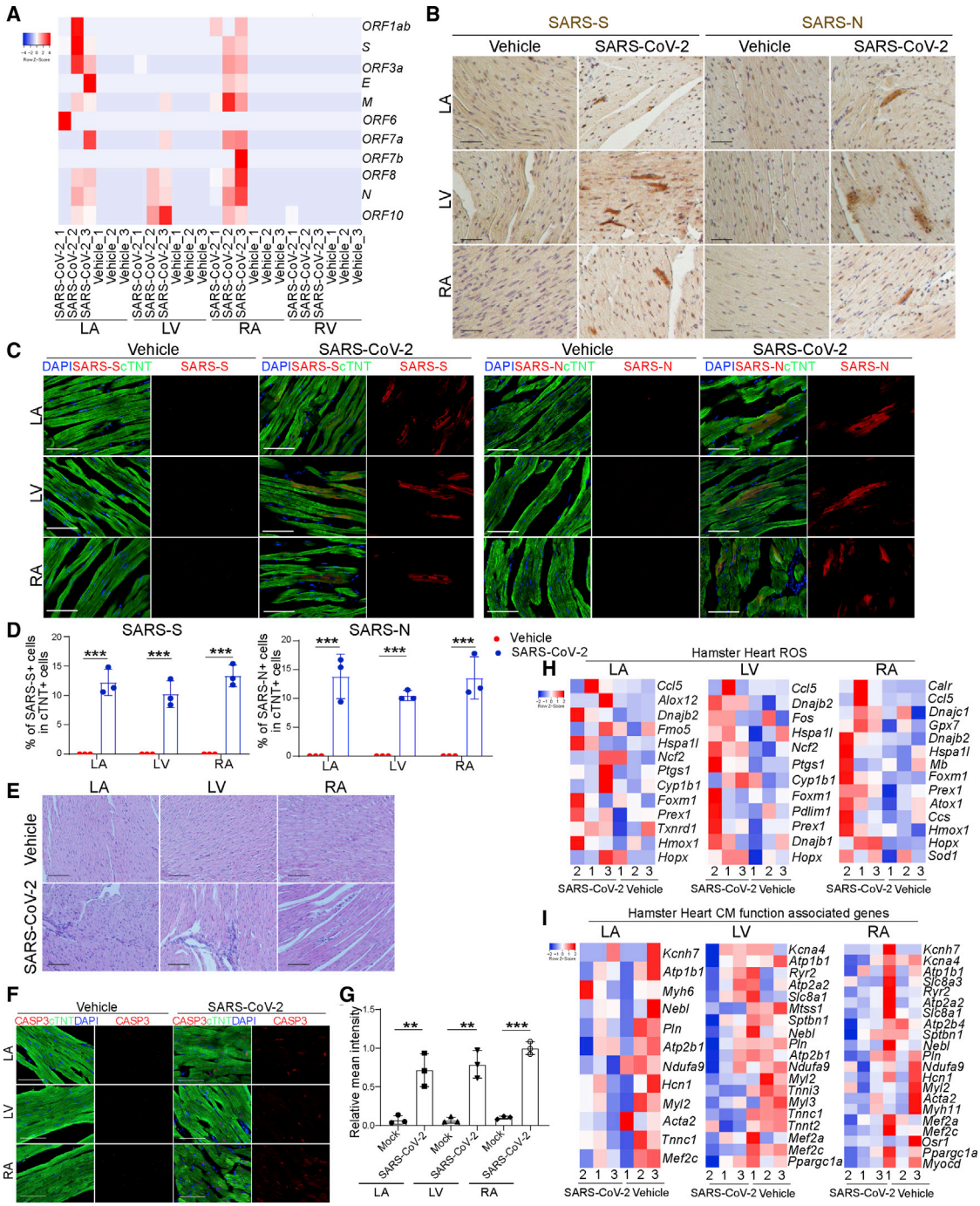

Figure 1. SARS-CoV-2 is detected in CMs of SARS-CoV-2-infected hamsters

(A) Heatmap of SARS-CoV-2 genes in heart tissues obtained from SARS-CoV-2-infected (n = 3) or mock-infected (n = 3) hamsters.

(B) Immunohistochemistry staining of viral spike and nucleocapsid protein in the LA, LV, and RA heart tissues of from uninfected (n = 3) or infected (n = 3) hamsters. Scale bar, 50 μm.

(C and D) Immunofluorescence staining (C) and the percentage (D) of spike^{+} and nucleocapsid^{+} cells in the LA, LV, and RA heart tissues from uninfected (n = 3) or infected (n = 3) hamsters. Scale bar, 50 μm.

(E) H&E staining of LA, LV, and RA heart tissues from uninfected (n = 3) or infected (n = 3) hamsters. Scale bar, 50 μm.

(F and G) Immunofluorescence staining (F) and the relative mean intensity of CASP3 (G) in cTNT^{+} cells in the LA, LV, and RA heart tissues obtained from SARS-CoV-2-infected (n = 3) or mock-infected (n = 3) hamsters. Scale bar, 50 μm.

(legend continued on next page)

observed SARS-CoV-2 virions in cardiac tissues of an 11-year-old child with multisystem inflammatory syndrome in children related to COVID-19 who developed cardiac failure and passed away 1 day after admission to the hospital. Another potential mechanism for cardiac damage could be mediated by immune cells. Although it has been controversial whether CMs are directly infected by SARS-CoV-2 in patients, several studies using COVID-19 post-mortem heart samples have consistently identified abnormal inflammatory infiltrates composed of $CD11b^+$ macrophages (Escher et al., 2020), $CD68^+$ macrophages (Lindner et al., 2020; Tavazzi et al., 2020), and, to a lesser extent, T cells (Yao et al., 2020).

Due to inherent challenges to collecting heart biopsies from COVID-19 patients during or after acute infection, we instead systematically examined heart tissues of SARS-CoV-2-infected Syrian hamsters (*Mesocricetus auratus*), an established and relevant animal model to study COVID-19 *in vivo*. We show that CMs of intranasally inoculated hamsters are infected leading to altered gene expression profiles associated with impaired CM function and increased reactive oxygen species (ROS), which was further confirmed in heart autopsies of COVID-19 patients. Using an immuno-cardiac co-culture platform with hPSC-derived CMs and monocytes/macrophages, we found that infected CMs recruit monocytes by secretion of CCL2 and that macrophage recruitment limits SARS-CoV-2 infection. This hPSC-based platform thus provides a useful new tool to model CM infection, immune cell infiltration, and cardiac histopathology of COVID-19 patients.

RESULTS

SARS-CoV-2 is detected in the CMs of SARS-CoV-2-infected hamsters

To examine the hearts of SARS-CoV-2-infected hamsters, 3- to 5-week-old male hamsters were intranasally inoculated with SARS-CoV-2. Forty-eight hours post infection (hpi), hamsters were euthanized and hearts were collected and separated into left ventricle (LV), left atrium (LA), right atrium (RA), and right ventricle (RV), followed by RNA sequencing (RNA-seq) analysis. SARS-CoV-2 transcripts were detected in hearts of six out of nine infected hamsters. Interestingly, viral transcripts were detected in LA, LV, and RA, but not RV (Figure 1A). SARS-CoV-2 spike and nucleocapsid protein were detected in CMs by immunohistochemistry (Figure 1B) and immunofluorescence staining (Figures 1C and 1D). Spike protein was also detected in $cTNT^-$ non-CMs (Figure S1A). Hematoxylin and eosin staining showed damaged cardiac tissue structure and infiltration of mononuclear cells in heart tissue from infected but not control animals (Figure 1E). Consistent with this tissue damage, we also observed significantly higher relative mean intensities of cleaved caspase-3 (CASP3) in $cTNT^+$ cells of LA, LV, and RA (Figures 1F and 1G), suggesting increased rates of apoptosis in CMs of infected hamsters. RNA-seq analysis revealed transcript profiles consistent with increased expression of ROS-related genes (Figure 1H) and decreased expression levels of CM function-associated genes (Figure 1I) in LA, RA, and LV. The gene expression changes were quite robust, even though a relatively small number of infected CMs and minimal myocardial damage were detected in the immunostaining assays.

To validate these findings in clinical COVID-19 cases, we compared heart autopsy samples from non-COVID-19 donors and four COVID-19 patients with cardiac symptoms. New EKG findings, including atrial fibrillation/paced rhythm and ST-segment or T-wave changes, were detected in three of the COVID-19 patients. Troponin was detected (0.51–1.83 ng/mL) in all four COVID-19 patients. Consistent with our observations in SARS-CoV-2-infected hamsters, hematoxylin and eosin staining showed damage to cardiac tissues as well as infiltration of mononuclear cells in heart sections of the COVID-19 patients (Figure 2A). Furthermore, increased expression of ROS-associated genes and decreased expression of CM function-associated genes was observed (Figures 2B and 2C). Finally, CASP3 expression in $cTNT^+$ cells of the COVID-19 patient samples was significantly higher than in samples from non-COVID-19 patients (Figures 2D and 2E), suggesting increased apoptosis of CMs in COVID-19 patients. Moreover, we also detected viral transcripts in heart tissue samples of COVID-19 patients (Figure S1B). Together, these data show evidence of SARS-CoV-2 cardiac infection and damage *in vivo*.

SARS-CoV-2-infected CMs lose cell identity and secrete CCL2

Our previous studies showed that hPSC-derived CMs are permissive to SARS-CoV-2 infection (Yang et al., 2020), which established a platform to model CM cellular response to SARS-CoV-2 infection. CMs were derived

(H and I) Heatmap of ROS-associated genes (H) and CM function-associated genes (I) in the LA, LV, and RA heart tissues obtained from SARS-CoV-2-infected (n = 3) or mock-infected (n = 3) hamsters.

All heatmap data are presented as the *Z* score. All graphed data are presented as mean ± SD. p values were calculated by unpaired two-tailed Student's t test. **p < 0.01, ***p < 0.001.

See also Figure S1.

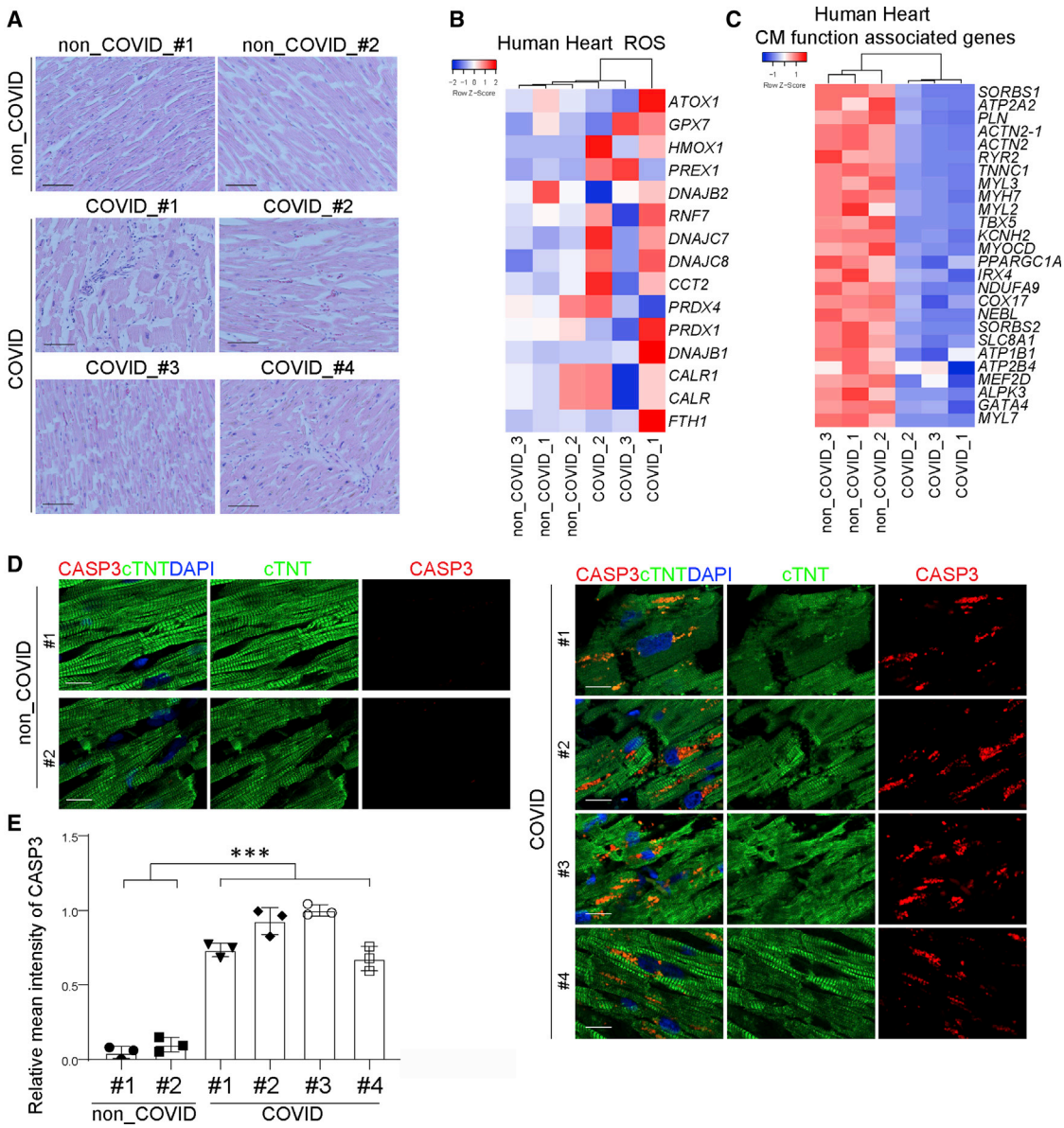

Figure 2. Analysis of autopsy heart samples of non-COVID-19 and COVID-19 patients

(A) H&E staining of autopsy heart samples of non-COVID-19 and COVID-19 patients (n = 2 non-COVID-19 subjects, n = 4 COVID-19 patients). Scale bar, 50 μm.

(B and C) Heatmap of ROS-associated genes (B) and CM function-associated genes (C) in autopsy heart samples of non-COVID-19 and COVID-19 patients (n = 3 non-COVID-19 subjects, n = 3 COVID-19 patients). Data are presented as the *Z* score.

(D and E) Immunofluorescence staining (D) and the relative mean intensity of CASP3 (E) in cTNT^{+} cells in autopsy heart samples of non-COVID-19 and COVID-19 patients (n = 2 non-COVID-19 subjects, n = 4 COVID-19 patients). Scale bar, 50 μm.

Data are presented as mean ± SD. p values were calculated by unpaired two-tailed Student's t test. ***p < 0.001.

See also Figure S1.

from an MYH6:mCherry H9 human embryonic stem cell (hESC) reporter line or an induced PSC (iPSC) line (Tsai et al., 2020) (Figure S2A). Over 90% of these cells expressed mCherry and/or stained positive with antibodies recognizing sarcomeric α-actinin and cTNT (Figure S2B). To better characterize the permissiveness of this hPSC-derived CM platform to SARS-CoV-2, we infected the hESC-derived CMs or iPSC-derived CMs with SARS-CoV-2 (USA-WA1/2020). We observed robust infection of CMs from both sources at 24–48 hpi based on subgenomic transcription

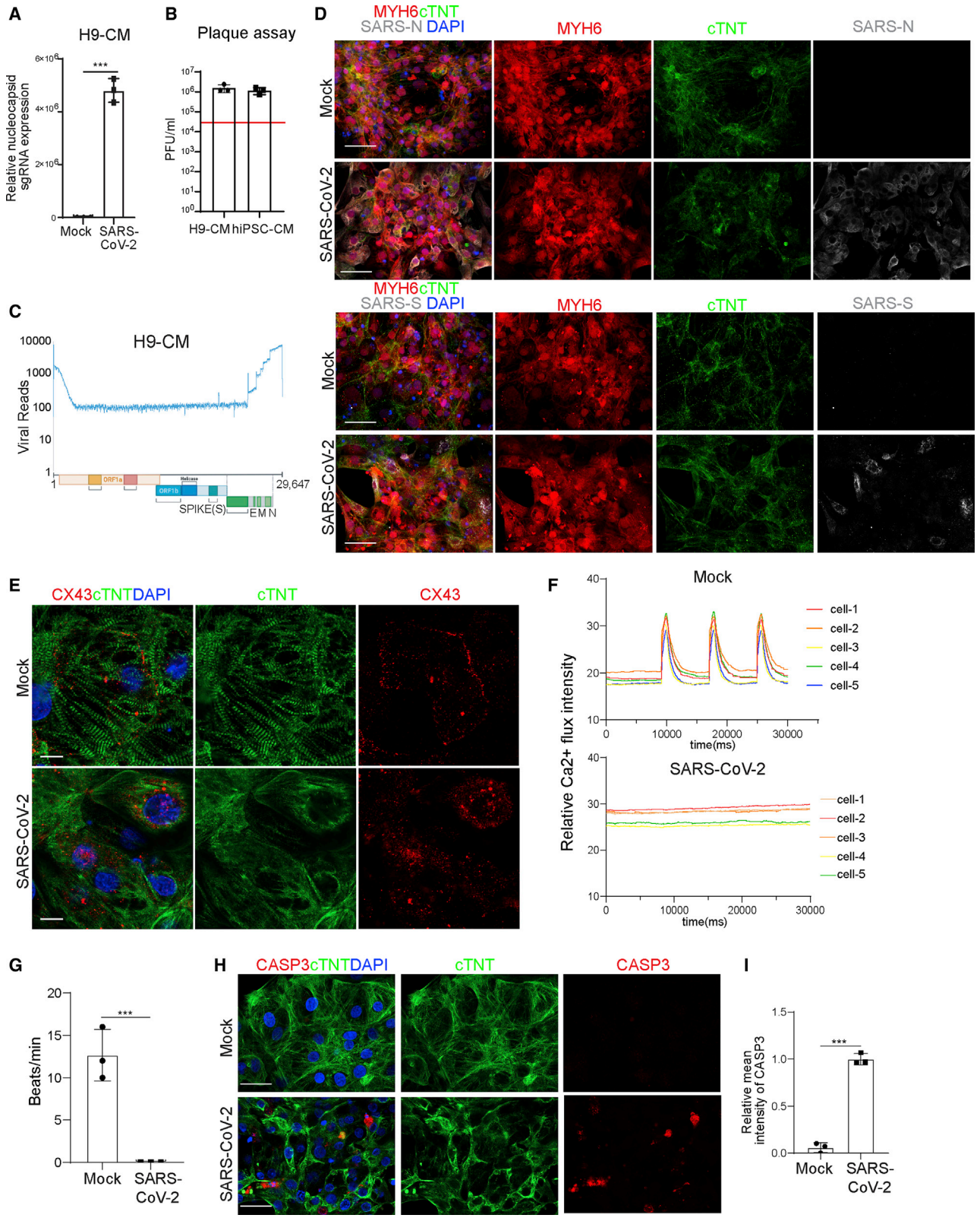

(legend on next page)

(Figures 3A and S3A) and the release of infectious viral particles (Figures 3B and S3B). At 72 hpi, both viral RNA and infectious viral titers decreased, which could be explained by the death of infected cells. Efficient replication in hPSC-derived CMs was demonstrated by full coverage of the viral genome by RNA-seq analysis (Figure 3C) as well as spike and nucleocapsid immunostaining (Figure 3D). In contrast to uninfected CMs, which show organized sarcomeres, SARS-CoV-2-infected CMs lose sarcomere structure (Figure 3E). Connexin 43 (CX43) was detected at the cell membranes of uninfected CMs, while it showed an internalized subcellular localization in SARS-CoV-2-infected CMs, suggesting the loss of gap junctions (Figure 3E). This also corresponded to a loss of Ca^{2+} influx for infected CMs, leading to the loss of beating (Figures 3F and 3G; Videos S1 and S2). Finally, increased CASP3 staining suggests an increased rate of apoptosis of SARS-CoV-2-infected CMs (Figures 3H and 3I).

RNA-seq analysis of H9 hESC-derived CMs showed significantly different host transcript profiles of mock and infected CMs (Figures 4A and 4B). Consistent with the host transcriptional response observed in heart autopsies from COVID-19 patients, infected H9 hESC-derived CMs demonstrated a robust induction of chemokines and cytokines, including *CCL2* (Figures 4C and 4D). KEGG pathway analysis of differentially expressed genes highlighted pathways involved in inflammatory and immune responses, including the tumor necrosis factor (TNF) signaling pathway, cytokine-cytokine receptor interaction, the nuclear factor κB signaling pathway, and the interleukin-17 (IL-17) signaling pathway (Figure 4E).

We also analyzed the response of adult human CMs to SARS-CoV-2 infection, to confirm responses are not specific to an hPSC-derived platform. Similar to hPSC-derived CMs, robust viral replication was detected in adult CMs (Figures 4F and 4G). In addition, the host transcriptional response to viral infection revealed a similar pattern, with robust induction of chemokines and cytokines, including CCL2 (Figures 4H–4K). KEGG pathway analysis highlighted pathways involved in inflammatory and immune responses, including the IL-17 signaling pathway, the TNF signaling pathway, the cytokine-cytokine receptor interaction, and the chemokine signaling pathway in the infected adult human CMs (Figure 4L). Finally, significantly increased protein levels of CCL2 were confirmed by ELISA in the medium of H9 hESC-derived CMs after SARS-CoV-2 infection, compared with mock-infected cells (Figure 4M), and higher *CCL2* expression levels were also detected in heart tissue samples from COVID-19 patients compared with those from non-COVID-19 patients (Figure 4N).

Ccl2 expression and macrophage infiltration in hearts of SARS-CoV-2-infected hamsters

To further investigate the role of Ccl2 in myocardial pathology, we examined Ccl2 expression in the hearts of SARS-CoV-2-infected hamsters. Consistent with our data in hPSC-derived CMs and human samples, the LA, LV, and RA of SARS-CoV-2-infected hamsters showed increased levels of *Ccl2* expression (Figure 5A), which was further validated by immunostaining (Figures 5B and 5C). Cell-mixture deconvolution using an LM22 matrix (Vallania et al., 2018) identified the enrichment of pro-inflammatory macrophages in the LA, LV, and RA of SARS-CoV-2-infected hamsters compared with controls (Figure 5D), which is consistent with previous reports of abnormal macrophage infiltration in hearts of COVID-19 patients (Escher et al., 2020; Lindner et al., 2020; Tavazzi et al., 2020; Yao et al., 2020). This was further confirmed by immunohistochemistry analysis showing an increase of $CD163^{+}$ macrophages

Figure 3. SARS-CoV-2 infection causes CM damage

(A) Relative abundance of viral subgenomic RNA (N) transcription in SARS-CoV-2-infected H9-derived CMs (24 hpi, MOI = 0.1, n = 3 independent experiments).

(B) Plaque assay of SARS-CoV-2-infected H9-derived CMs and iPSC-derived CMs (24 hpi, MOI = 0.1). The red line indicates the input virus: 4×10^4 pfu.

(C) Read alignment to the SARS-CoV-2 genome after RNA-seq analysis of SARS-CoV-2-infected H9-derived CMs (24 hpi, MOI = 0.1, n = 3 independent experiments). Schematic denotes the SARS-CoV-2 genome.

(D) Immunofluorescence staining using viral spike and nucleocapsid antibodies in SARS-CoV-2-infected H9-derived CMs (24 hpi, MOI = 0.1, n = 3 independent experiments). Scale bar, 50 μm.

(E) Immunofluorescence staining using cTNT and CX43 antibodies on mock or SARS-CoV-2-infected H9-derived CMs at 24 hpi (MOI = 0.1, n = 3 independent experiments). Scale bar, 10 μm.

(F) Quantification of Ca^{2+} flux intensity of mock or SARS-CoV-2-infected H9-derived CMs at 48 hpi (MOI = 0.1, n = 3 independent experiments). Each condition shows five cells.

(G) Beating rate of mock- or SARS-CoV-2-infected H9-derived CMs at 48 hpi (MOI = 0.1, n = 3 independent experiments).

(H and I) Immunofluorescence staining (H) and the relative mean intensity of CASP3 (I) in $cTNT^{+}$ cells of mock- or SARS-CoV-2-infected H9-derived CMs at 24 hpi (MOI = 0.1, n = 3 independent experiments). Scale bar, 50 μm.

Data are presented as mean ± SD. p values were calculated by unpaired two-tailed Student's t test. ***$p < 0.001$.

See also Figures S2 and S3 and Videos S1 and S2.

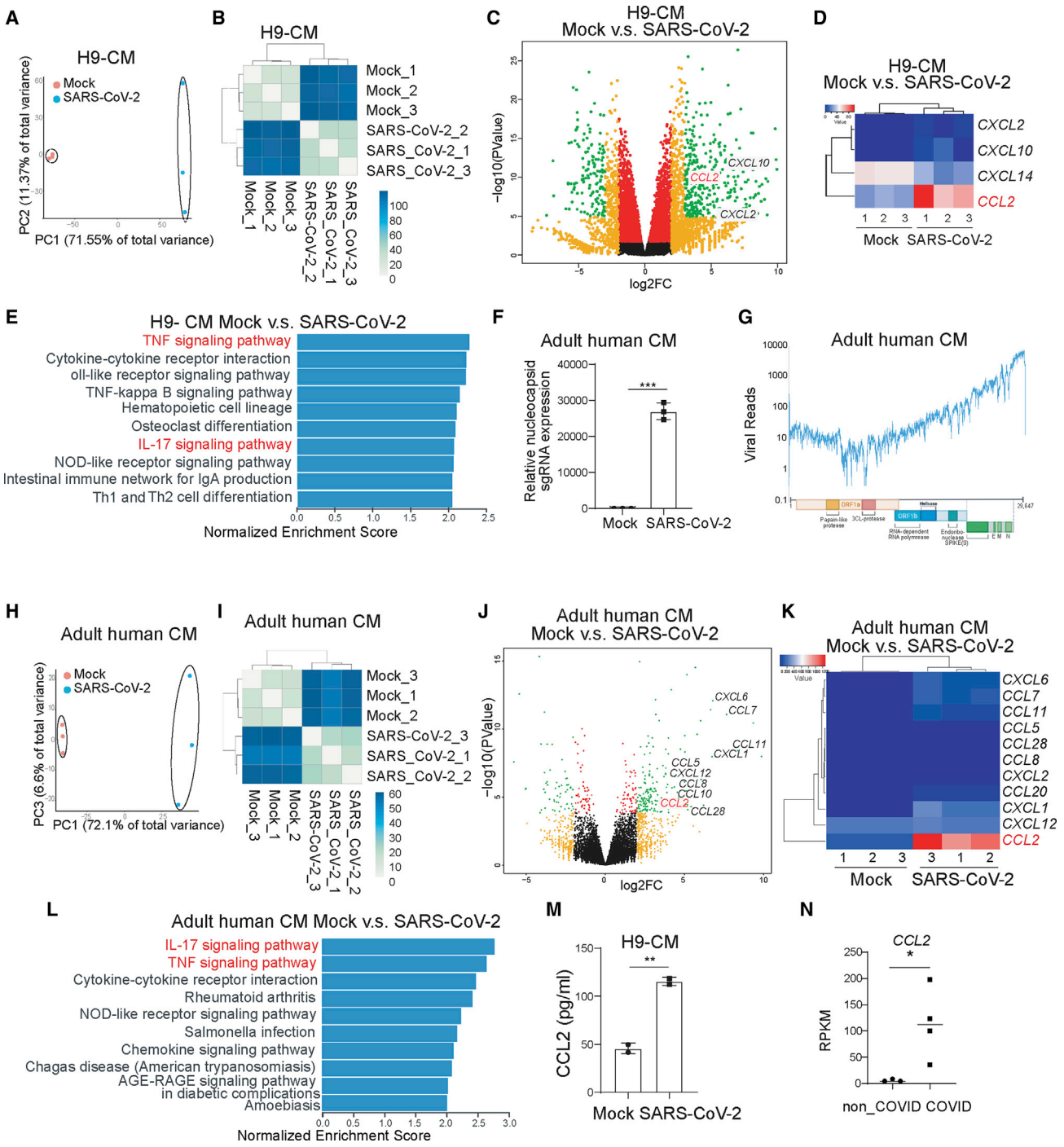

Figure 4. CMs secrete CCL2 upon SARS-CoV-2 infection

(A and B) Principal-component analysis (PCA) plot (A) and heatmap (B) analysis of H9-derived CMs infected with SARS-CoV-2 virus or mock infected at 24 hpi (MOI = 0.1, n = 3 independent experiments).

(C and D) Volcano plot (C) and heatmap (D) analysis of chemokines expressed by H9-derived CMs infected with SARS-CoV-2 virus or mock at 24 hpi (MOI = 0.1, n = 3 independent experiments). Colored dots labeled correspond to chemokines with significant ($p < 0.05$) and greater than 2-fold expression level changes.

(E) KEGG analysis of H9-derived CMs infected with SARS-CoV-2 virus or mock at 24 hpi (MOI = 0.1, n = 3 independent experiments).

(legend continued on next page)

in the LA, LV, and RA of SARS-CoV-2-infected hamsters (Figures 5E and 5F).

SARS-CoV-2-infected CMs recruit monocytes by secreting CCL2

Macrophages include tissue-resident macrophages and migrating macrophages (Ginhoux and Jung, 2014). Migrating macrophages are usually derived from monocytes in the blood. During inflammation, circulating monocytes leave the bloodstream and migrate into tissues where, following conditioning by local growth factors, pro-inflammatory cytokines, and microbial products, they differentiate into macrophages (Shi et al., 2020).

We therefore examined the ability of SARS-CoV-2-infected CMs to stimulate migration of monocytes. Monocytes were derived from the same parental H9- or H1-hESC lines following a previously reported protocol (Cao et al., 2019) (Figure S4A) through a stepwise manner, including the generation of mesodermal cells, followed by hematopoietic progenitor cells, monocytes (Figure S4B), and finally $CD14^{+}/CD11B^{+}$ macrophages (Figure S4C). To determine whether these hPSC-derived macrophages are susceptible to SARS-CoV-2 infection, H9- or H1-hESC-derived macrophages were infected with SARS-CoV-2. However, viral replication was detected neither by qRT-PCR nor plaque assay, suggesting that macrophages are not productively infected by SARS-CoV-2 (Figures S4D and S4E).

Next, we analyzed the ability of infected CMs to recruit monocytes to the site of infection. To that end, we plated hPSC-derived CMs at the bottom and hPSC-derived monocytes at the top of a transwell plate and infected the CMs at the bottom of the plate (Figure 6A). Monocyte migration was quantified 24 hpi by crystal violet staining. The number of monocytes that migrated was significantly higher when cultured with SARS-CoV-2-infected CMs compared with when cultured with mock-infected hPSC-derived CMs using monocytes derived from either of the two hESC lines, indicating that SARS-CoV-2-infected CMs recruit monocytes (Figures 6B, 6C, S5A, and S5B).

We next tested whether adult human CMs infected with SARS-CoV-2 also recruit monocytes. Consistent with experiments using hPSC-derived CMs, monocytes were recruited at a significantly enhanced rate when cultured with SARS-CoV-2-infected adult human CMs than when cultured with mock-infected adult human CMs (Figures 6D, 6E, S5C, and S5D).

We previously showed that infected CMs secrete significant levels of CCL2. Therefore, to determine whether CCL2 is sufficient to induce monocyte migration, CCL2 was added to the bottom of a transwell plate with monocytes cultured at the top. Indeed, significantly more monocytes were found in CCL2 containing media than in untreated media (Figures 6F, 6G, S5E, and S5F). To determine whether CCL2 is the key driver for monocyte migration, hPSC-derived CMs or adult human CMs were cultured as before with monocytes in transwell plates and SARS-CoV-2 infections were performed in the absence or presence of CCL2-neutralizing antibodies or CCR2 inhibitors (Figures 6H–6K and S5G–S5J). Interestingly, the recruitment of monocytes by infected CMs was significantly inhibited if CCL2 signaling was disrupted, either by neutralizing CCL2 antibodies or by inhibition of the CCL2 receptor CCR2. Together, these data suggest that SARS-CoV-2 infection of CMs induces CCL2 secretion, which recruits monocytes.

Co-culture of hPSC-derived CMs and macrophages reveals that macrophages decrease SARS-CoV-2-infected CMs

We next investigated how recruited macrophages affect viral infection. To model the viral entry process, we created an immunocardiac co-culture platform containing hPSC-derived CMs and hPSC-derived macrophages and infected

(F) Relative subgenomic RNA (N) transcription in adult human CMs at 24 hpi of SARS-CoV-2 virus at 24 hpi (MOI = 0.1, n = 3 independent experiments).
(G) Alignment of the transcriptome with the viral genome in SARS-CoV-2-infected adult human CMs at 24 hpi (MOI = 0.1, n = 3 independent experiments). Schematic denotes the SARS-CoV-2 genome.
(H and I) PCA plot (H) and heatmap (I) analysis of adult human CMs infected with SARS-CoV-2 virus or mock at 24 hpi (MOI = 0.1, n = 3 independent experiments).
(J and K) Volcano plot (J) and heatmap (K) analysis of chemokines expressed by adult human CMs infected with SARS-CoV-2 virus or mock infected at 24 hpi (MOI = 0.1, n = 3 independent experiments). Colored dots labeled correspond to chemokines with significant ($p < 0.05$) and greater than 2-fold expression level changes.
(L) KEGG analysis of adult human CMs infected with SARS-CoV-2 virus or mock infected at 24 hpi (MOI = 0.1, n = 3 independent experiments).
(M) ELISA was performed to examine the protein level of CCL2 in H9-derived CMs infected with SARS-CoV-2 virus or mock infected at 24 hpi (MOI = 0.1, n = 3 independent experiments).
(N) *CCL2* transcript levels in autopsy heart samples of non-COVID-19 and COVID-19 patients (n = 3 non-COVID-19 subjects, n = 4 COVID-19 patients). RPKM, reads per kilobase of transcript, per million mapped reads.
Data are presented as mean ± SD. p values were calculated by unpaired two-tailed Student's t test. *$p < 0.05$, **$p < 0.01$.

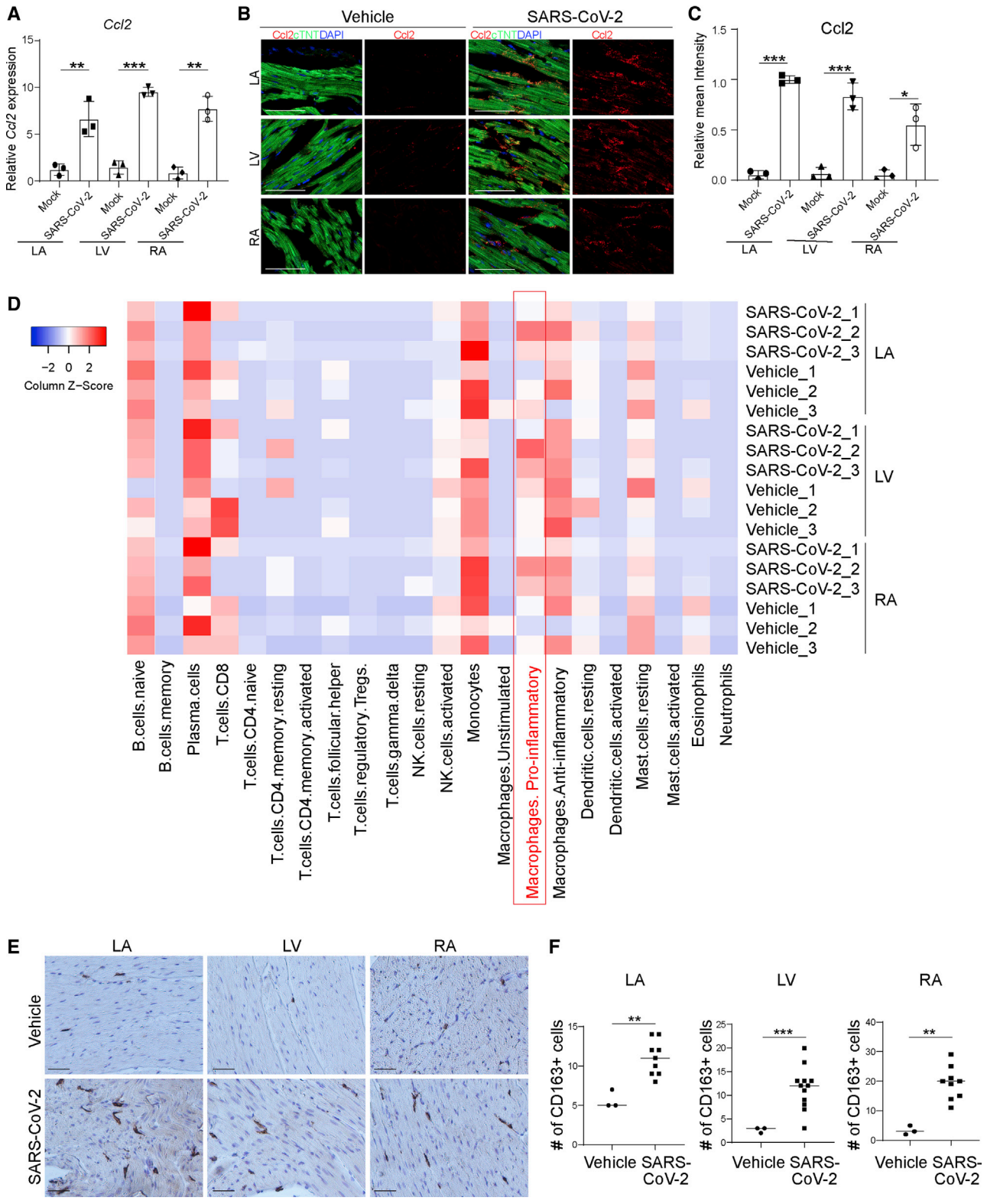

Figure 5. Pro-inflammatory macrophages are enriched in hearts of SARS-CoV-2-infected hamsters

(A) Relative expression levels of *Ccl2* in LA, LV, and RA heart tissues obtained from SARS-CoV-2-infected hamsters (n = 3) and mock-infected hamsters (n = 3).

(legend continued on next page)

it with a SARS-CoV-2 spike protein pseudovirus carrying a luciferase (Luc) reporter. Notably, in the presence of macrophages Luc activity was significantly decreased in a dose-dependent manner (Figures S6A and S6B). Immunostaining further confirmed the decrease of Luc^+ cells in $MYH6{:}mCherry^+$ cells (Figures S6C and S6D).

The immunocardiac co-culture was further examined by single-cell RNA-seq (scRNA-seq). The transcript profiling data were projected using Uniform Manifold Approximation and Projection. In the virus-infected immunocardiac co-culture platform, four distinct cell clusters were identified: CMs, macrophages, stem/progenitor cells, and one cluster expressing both CM and macrophage markers (Figure 7A). The expression of marker genes, including *MYH6*, *MYH7*, and *TNNT2* (CMs), and *CD163* and *CD68* (macrophages), and *GATA6* (progenitor cells) in each cell population confirmed the robustness of the cell-type classification strategy (Figures 7B, S6E, and S6F).

ACE2, the gene encoding the main cellular receptor for SARS-CoV-2, is mainly expressed in hPSC-derived CMs and cardiac progenitors (Figures S6G and S6H). The effector protease *TMPRSS2* (Hoffmann et al., 2020) is not expressed in hPSC-derived CMs and only rarely expressed in hPSC-derived cardiac progenitors (Figures S6G and S6H). However, *FURIN*, the gene encoding a pro-protein convertase that pre-activates SARS-CoV-2 (Shang et al., 2020), and *CTSL*, the gene encoding cathepsin L, a proteinase that might be able to substitute for TMPRSS2 (Hoffmann et al., 2020), are highly expressed in both hPSC-derived CMs and cardiac progenitors.

Transcripts deriving from the pseudovirus, including *Luc*, were detected in infected CMs, but only at very low levels in macrophages (Figure S6I), which is consistent with our previous report (Yang et al., 2020). The cell cluster that expressed both CM and macrophage markers and, in addition, high levels of viral transcripts, likely represents infected CMs engulfed by macrophages (Figure 7C). *Luc* expression in CMs was significantly lower in the presence of co-cultured macrophages (Figures 7D and 7E). Consistently, infected CMs showed increased expression of CCL2, which was further elevated in the presence of macrophages (Figures S6J and S6K).

To further validate the impact of macrophages on SARS-CoV-2 infection, the immunocardiac co-culture platform containing hPSC-derived CMs and hPSC-derived macrophages was infected with SARS-CoV-2. In agreement with our previous findings, we found that viral sgRNA transcripts were significantly decreased after viral infection in the co-culture relative to the CM marker *cTNT* (Figure 7F). This was further confirmed by a decrease in viral nucleocapsid expression in $cTNT^+$ cells (Figures 7G, 7H, S6L, and S6M). In hPSC-derived CMs and macrophages that were co-cultured long term for 1 week the same phenomenon was observed (Figures 7I and 7J). Together, these data suggest that macrophages play an active role in limiting the extent of SARS-CoV-2 infection potentially by engulfing infected CMs.

DISCUSSION

Myocardial injury has been reported in COVID-19 patients and is associated with increased mortality (Ruan et al., 2020; Zhou et al., 2020), yet the cause of myocardial injury has not been characterized or elucidated. Recent studies using SARS-CoV-2 hACE2 transgenic mice or hPSC-derived CMs reported the detection of viral RNA in the mouse heart or in infected CMs (Jiang et al., 2020). In addition, viral RNA has been detected in heart autopsies of COVID-19 patients by several groups (Escher et al., 2020; Lindner et al., 2020). However, SARS-CoV-2 virions have largely been detected in interstitial cells of the myocardium in COVID-19 patient samples (Lindner et al., 2020; Tavazzi et al., 2020). A recent study reported the detection of viral antigen and RNA in CMs in hearts of COVID-19 patients (Bulfamante et al., 2020). Here, using intranasally infected hamsters, a relevant animal model for COVID-19, we clearly detected viral protein expression in CMs of infected animals. This provides direct evidence that intranasal exposure of SARS-CoV-2 leads to infection of CMs *in vivo*. Although CMs and other cardiac cells can be infected by SARS-CoV-2, other mechanisms, such as respiratory failure, hypoxemia, and hyper-inflammation caused by cytokines released by the macrophages recruited to the heart, may also contribute to the heart damage seen in COVID-19 patients.

CCL2 expression levels were significantly upregulated in infected hPSC-derived CMs and adult CMs, and in the hearts of SARS-CoV-2-infected hamsters. We also examined *CCL2* expression levels after SARS-CoV-2 infection in hPSC-derived lung organoids (Han et al., 2021) or hPSC-

(B and C) Immunofluorescence staining (B) and quantification (C) of Ccl2 in LA, LV, and RA heart tissues obtained from SARS-CoV-2-infected hamsters (n = 3) and mock-infected hamsters (n = 3). Scale bar, 50 μm.

(D) Cell-mixture deconvolution identified the enrichment of immune cells in the LA, LV, and RA of SARS-CoV-2-infected hamsters (n = 3) compared with mock-infected hamsters (n = 3).

(E and F) Immunohistochemistry staining (E) and quantification (F) of $CD163^+$ cells in LA, LV, and RA heart tissues obtained from SARS-CoV-2-infected hamsters (n = 3) and mock-infected hamsters (n = 3). Scale bar, 50 μm.

Data are presented as mean ± SD. p values were calculated by unpaired two-tailed Student's t test. *p < 0.05, **p < 0.01, ***p < 0.001.

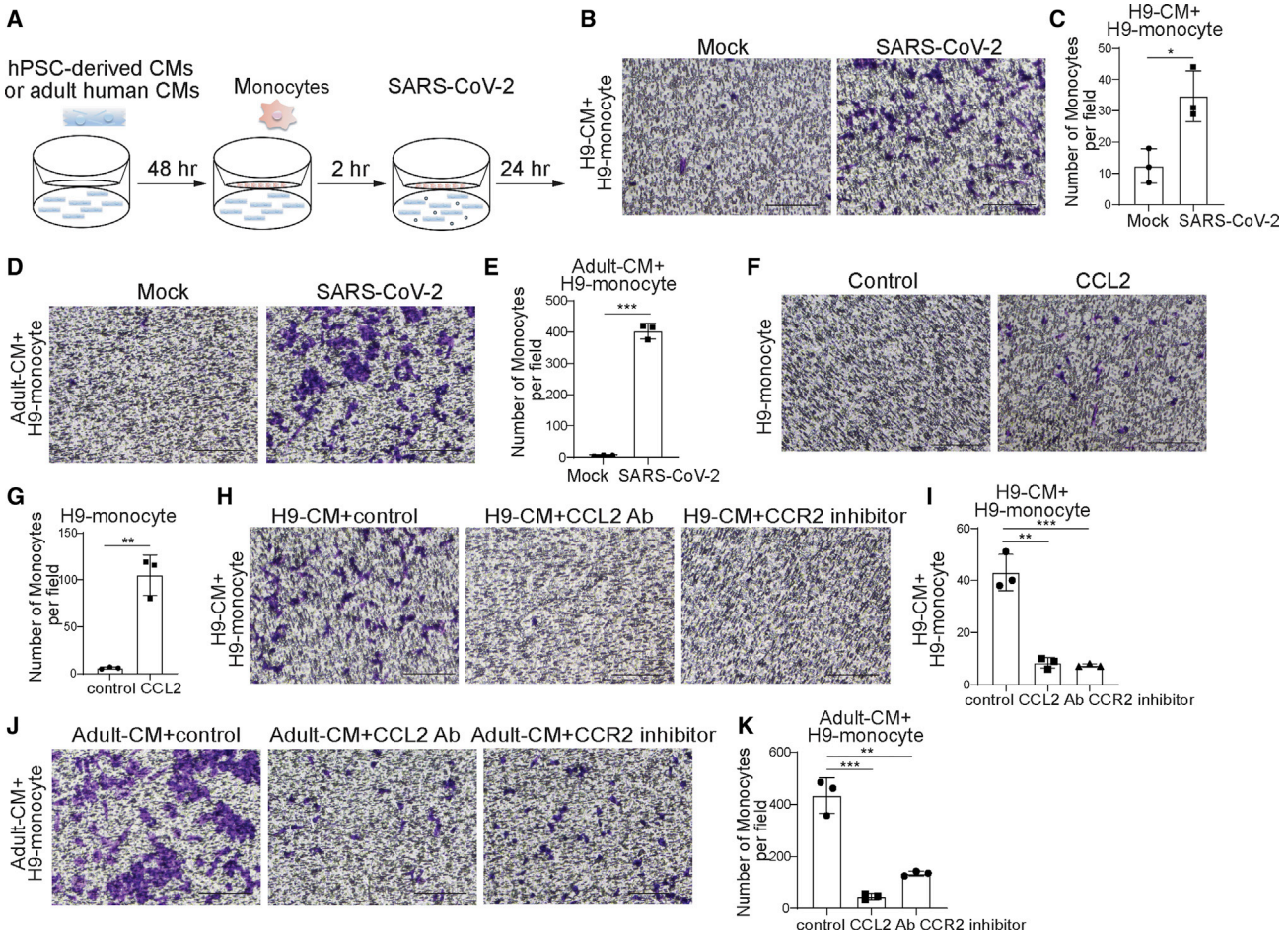

Figure 6. CMs recruit monocytes following SARS-CoV-2 infection through secreting CCL2

(A) Scheme of the monocyte recruitment assay using hPSC-derived CMs or adult human CMs and hPSC-derived monocytes in the presence of SARS-CoV-2 infection

(B and C) Phase contrast images (B) and quantification (C) of migrated H9-derived monocytes recruited by H9-derived CMs infected with SARS-CoV-2 virus or mock infected in the monocyte migration assay (MOI = 0.1, n = 3 independent experiments). Scale bar, 100 μm.

(D and E) Phase contrast images (D) and quantification (E) of H9-derived monocytes recruited by adult human CMs infected with SARS-CoV-2 virus or mock infected in the monocyte recruitment assay (MOI = 0.1, n = 3 independent experiments). Scale bar, 100 μm.

(F and G) Phase contrast images (F) and quantification (G) of migrated H9-derived monocytes recruited by CCL2 in the monocyte recruitment assay (n = 3 independent experiments). Scale bar, 100 μm.

(H and I) Phase contrast images (H) and quantification (I) of migrated H9-derived monocytes recruited by H9-derived CMs infected with SARS-CoV-2 virus and treated with CCL2-neutralizing antibody or CCR2 inhibitor (RS504393) in the monocyte recruitment assay (MOI = 0.1, n = 3 independent experiments). Scale bar, 100 μm.

(J and K) Phase contrast images (J) and quantification (K) of migrated H9-derived monocytes recruited by adult human CMs infected with SARS-CoV-2 virus and treated with CCL2-neutralizing antibody or CCR2 inhibitor in the monocyte recruitment assay (MOI = 0.1, n = 3 independent experiments). Scale bar, 100 μm.

Data are presented as mean ± SD. p values were calculated by unpaired two-tailed Student's t test. *$p < 0.05$, **$p < 0.01$, ***$p < 0.001$. See also Figures S4 and S5.

derived pancreatic endocrine cells (Yang et al., 2020), and in lung autopsies of non-COVID-19 versus COVID-19 patients (Han et al., 2021) (Figure S7A). *CCL2* levels are upregulated in both SARS-CoV-2-infected cells/organoids and COVID-19 patient lung autopsy samples. However, when we examined *CCL2* expression levels in idiopathic dilated cardiomyopathy LV tissue, ischemic LV tissue, or murine encephalomyelitis virus-infected CMs (Figure S7B, GSE57338 and GSE119860), *CCL2* expression was not significantly increased compared with non-failing LV tissue

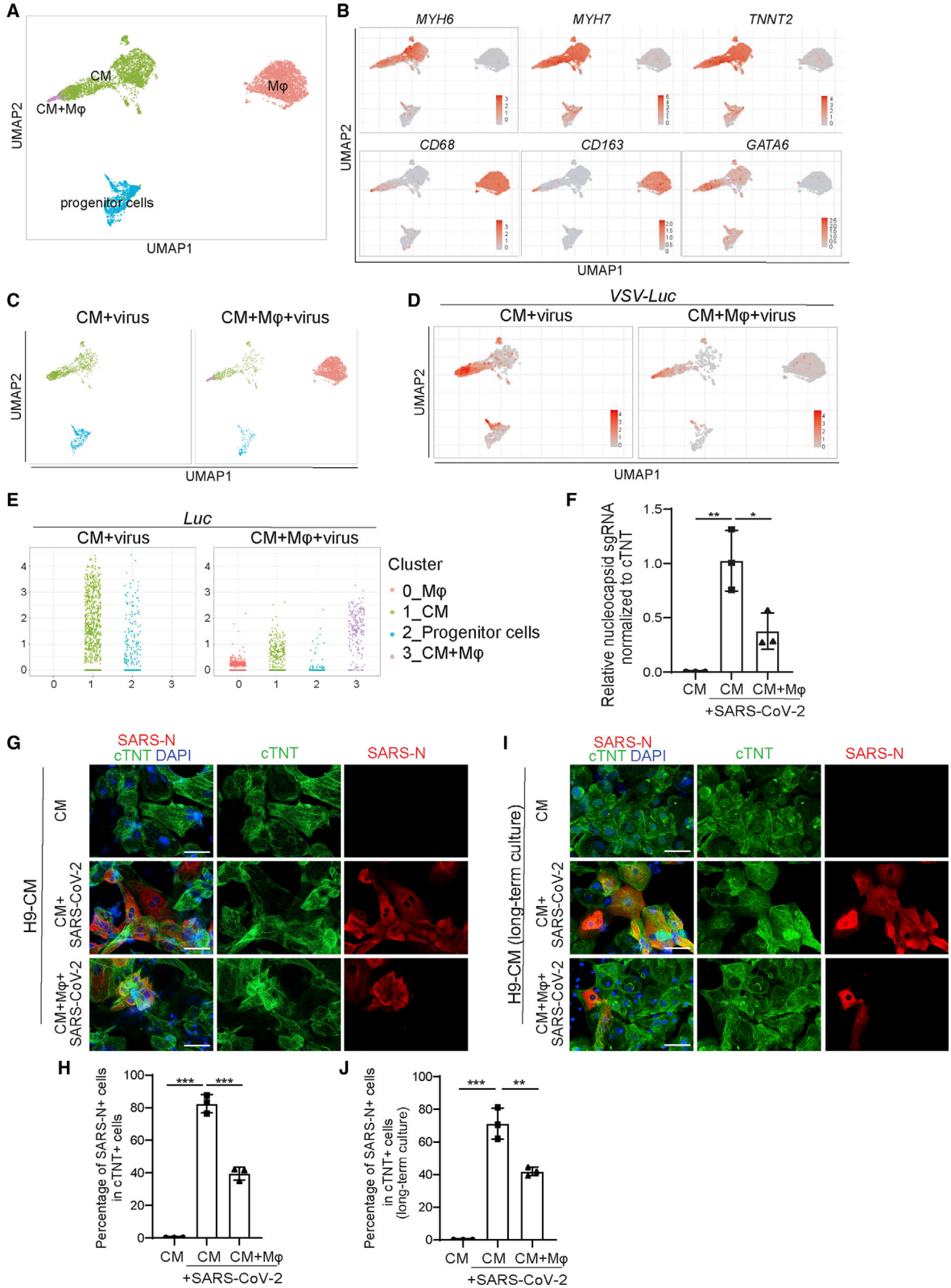

(legend on next page)

or uninfected CMs. This suggests that *CCL2* is not upregulated by any cardiac damage but more specifically in the condition of SARS-CoV-2 infection. Moreover, we found that SARS-CoV-2-infected CMs expressed higher levels of CCL2 than non-infected cells in the hamster model according to scRNA-seq data (Figures S7C–S7E).

CCL2, also known as monocyte chemoattractant protein 1, is a chemokine that facilitates the migration and infiltration of monocytes/macrophages to sites of inflammation produced by either tissue injury or infection (Bose and Cho, 2013). Using a transwell platform, we showed that hPSC-derived CMs or adult human CMs infected with SARS-CoV-2 recruit monocytes. This is consistent with previous reports of abnormal macrophage infiltration in hearts of COVID-19 patients (Escher et al., 2020; Lindner et al., 2020; Tavazzi et al., 2020; Yao et al., 2020).

Finally, we created a co-culture platform using hPSC-derived CMs and macrophages to study the impact of macrophages on infected CMs. scRNA-seq data suggested that the presence of macrophages decreases SARS-CoV-2-infected CMs. This might be due to increased apoptosis of SARS-CoV-2-infected CMs or engulfing of virus by macrophages. In the absence of SARS-CoV-2, the presence of macrophages does not affect CM survival (Figures S7F and S7G). However, in the context of COVID-19, macrophages might be considered a "double-edged sword." When CMs are infected with SARS-CoV-2, recruitment of macrophages can promote secretion of inflammatory cytokines, ROS, and cause CM damage. On the other hand, engulfing of virus by macrophages (and likely engulfment of infected CMs), limits the infection of CMs. Indeed, cell-mixture deconvolution identified the enrichment of pro-inflammatory macrophages in the LA, LV, and RA of SARS-CoV-2-infected hamsters. In addition, ROS was upregulated in the hearts of infected hamsters, suggesting that macrophages recruited by CMs might also contribute to immune-mediated CM inflammatory damage in COVID-19 patients. Together, both direct CM infection and recruitment of immune cells, such as mononuclear cells, might contribute to balancing cardiac pathophysiology in COVID-19 patients. We cannot exclude the possibility that other types of cells in hearts can also be infected by SARS-CoV-2, as discussed in a recent perspective review (Yiangou et al., 2021) and contribute to monocyte recruitment. In addition, systemic conditions (e.g., inflammation, fever, nutrients, dehydration) might also contribute to heart damage. In summary, we report direct evidence of SARS-CoV-2 infection of CMs *in vivo* and established an *in vitro* model to study immune cell infiltration and pathophysiology in cardiac tissue of COVID-19 patients.

EXPERIMENTAL PROCEDURES

Details are provided in the supplemental experimental procedures.

Propagation and titration of SARS-CoV-2

SARS-CoV-2, isolate USA-WA1/2020 (NR-52281) was deposited by the Center for Disease Control and Prevention and obtained through BEI Resources, NIAID, NIH. Full details are available in the supplemental information.

SARS-CoV-2 infections of hamsters

Three- to five-week-old male Golden Syrian hamsters (*Mesocricetus auratus*) were obtained from Charles River. Hamsters were acclimated to the CDC/USDA-approved BSL-3 facility of the Global Health and Emerging Pathogens Institute at the Icahn School of Medicine at Mount Sinai for 2–4 days. Full details are available in the supplemental information.

Figure 7. A virus-immunocardiac co-culture platform reveals that hPSC-derived macrophages limit infection of SARS-CoV-2 CMs

(A) Uniform Manifold Approximation and Projection (UMAP) analysis of the virus-immunocardiac tissue platform containing hPSC-derived CMs and macrophages.

(B) UMAP of hPSC-derived CM and macrophage-related markers differentially expressed in each cluster. Relative expression levels of each marker gene ranged from low (gray) to high (red) as indicated.

(C) UMAP analysis of clusters in hPSC-derived CMs infected with SARS-CoV-2 entry virus (CM + virus) and the virus-immunocardiac tissue platform containing hPSC-derived CMs and macrophages infected with SARS-CoV-2 entry virus (CM + macrophage + virus).

(D) UMAP analysis of *Luc* expression in hPSC-derived CMs infected with SARS-CoV-2 entry virus (CM + virus) and the virus-immunocardiac tissue platform containing hPSC-derived CMs and macrophages infected with SARS-CoV-2 entry virus (CM + macrophage + virus).

(E) Jitter plot of *Luc* expression in hPSC-derived CMs infected with SARS-CoV-2 entry virus (CM + virus) and the virus-immunocardiac tissue platform containing hPSC-derived CMs and macrophages and infected with SARS-CoV-2 entry virus (CM + macrophage + virus).

(F) qRT-PCR analysis at 24 hpi of hPSC-derived CMs infected with mock or SARS-CoV-2 in the presence or absence of macrophages (MOI = 0.1, n = 3 independent experiments).

(G and H) Immunostaining (G) and quantification (H) of hPSC-derived CMs at 24 hpi with mock or SARS-CoV-2 in the presence or absence of macrophages for short-time co-culture (24 h, MOI = 0.1, n = 3 independent experiments). Scale bar, 50 μm.

(I and J) Immunostaining (I) and quantification (J) of hPSC-derived CMs at 24 hpi with mock or SARS-CoV-2 in the presence or absence of macrophages for long-time co-culture (7 days, MOI = 0.1, n = 3 independent experiments). Scale bar, 50 μm.

Data are presented as mean ± SD. p values were calculated by unpaired two-tailed Student's t test. *p < 0.05, **p < 0.01, ***p < 0.001. See also Figures S6 and S7.

Human studies

Tissue samples were provided by the Weill Cornell Medicine Department of Pathology. The Tissue Procurement Facility operates under an institutional review board-approved protocol and follows guidelines set by HIPAA. Full details are available in the supplemental information.

Data and code availability

scRNA-seq and RNA-seq data are available from the GEO repository database under accession number GSE151880.

SUPPLEMENTAL INFORMATION

Supplemental information can be found online at https://doi.org/10.1016/j.stemcr.2021.07.012.

AUTHOR CONTRIBUTIONS

S.C., T.E., B.R.t., R.E.S., and D.D.H. conceived and designed the experiments. L.Y., Y. Han., F.J., and J.Z. performed CM, macrophage differentiation, co-culture, and immunostaining. M.G. and J.K.L. performed ELISA analysis. P.W. and Y. Huang. provided SARS2-CoV-2 pseudo-entry virus. A.B., Y.B., C.R., and V.C. analyzed human samples. B.E.N.-P., R.M., L.C., S. Horiuchi., and B.R.t. performed SARS-CoV-2-related experiments. J.Z., T.Z., D.R., S. Houghton., and J.X. performed the scRNA-seq and bioinformatics analyses.

CONFLICTS OF INTEREST

S.C. is a member of editorial board of *Stem Cell Reports*. R.E.S. is on the scientific advisory board of Miromatrix Inc and is a paid consultant and speaker for Alnylam Inc. The other authors have no conflict of interest.

ACKNOWLEDGMENTS

This work was supported by the American Heart Association (18CSA34080171 to S.C. and T.E.), NIDDK (R01DK130454, R01DK116075, R01DK119667, R01DK119667-02S1, R01 DK124463, and U01 DK127777, S.C.), American Diabetes Association (7-20-COVID-211 to S.C.), Department of Surgery, Weill Cornell Medicine (to T.E. and S.C.), Bill and Melinda Gates Foundation (S.C., T.E., R.E.S, B.tO,) and (NCI R01CA234614, NIAID 2R01AI107301 and NIDDK R01DK121072 and 1RO3DK117252), Department of Medicine, Weill Cornell Medicine (to R.E.S.), by the Defense Advanced Research Projects Agency (DARPA-16-35-INTERCEPT-FP-006 to B.T.), and by the Jack Ma Foundation (to D.D.H.). S.C. and R.E.S. are supported as Irma Hirschl Trust Research Award Scholars. T.E. is supported by an Outstanding Investigator Award from the NHLBI (R35 HL135778). R.M. is supported by American Heart Association grant #833781. Y.H. is a NYSTEM Stem Cell Biology Scholar.

Received: July 6, 2021
Revised: July 15, 2021
Accepted: July 16, 2021
Published: September 14, 2021; corrected online: September 21, 2021

REFERENCES

Bojkova, D., Wagner, J.U.G., Shumliakivska, M., Aslan, G.S., Saleem, U., Hansen, A., Luxan, G., Gunther, S., Pham, M.D., Krishnan, J., et al. (2020). SARS-CoV-2 infects and induces cytotoxic effects in human cardiomyocytes. Cardiovasc. Res. https://doi.org/10.1093/cvr/cvaa267.

Bose, S., and Cho, J. (2013). Role of chemokine CCL2 and its receptor CCR2 in neurodegenerative diseases. Arch. Pharm. Res. *36*, 1039–1050. https://doi.org/10.1007/s12272-013-0161-z.

Bulfamante, G.P., Perrucci, G.L., Falleni, M., Sommariva, E., Tosi, D., Martinelli, C., Songia, P., Poggio, P., Carugo, S., and Pompilio, G. (2020). Evidence of SARS-CoV-2 transcriptional activity in cardiomyocytes of COVID-19 patients without clinical signs of cardiac involvement. Biomedicines *8*. https://doi.org/10.3390/biomedicines8120626.

Cao, X., Yakala, G.K., van den Hil, F.E., Cochrane, A., Mummery, C.L., and Orlova, V.V. (2019). Differentiation and functional comparison of monocytes and macrophages from hiPSCs with peripheral blood derivatives. Stem Cell Reports *12*, 1282–1297. https://doi.org/10.1016/j.stemcr.2019.05.003.

Dolhnikoff, M., Ferreira Ferranti, J., de Almeida Monteiro, R.A., Duarte-Neto, A.N., Soares Gomes-Gouvea, M., Viu Degaspare, N., Figueiredo Delgado, A., Montanari Fiorita, C., Nunes Leal, G., Rodrigues, R.M., et al. (2020). SARS-CoV-2 in cardiac tissue of a child with COVID-19-related multisystem inflammatory syndrome. Lancet Child Adolesc. Health *4*, 790–794. https://doi.org/10.1016/S2352-4642(20)30257-1.

Escher, F., Pietsch, H., Aleshcheva, G., Bock, T., Baumeier, C., Elsaesser, A., Wenzel, P., Hamm, C., Westenfeld, R., Schultheiss, M., et al. (2020). Detection of viral SARS-CoV-2 genomes and histopathological changes in endomyocardial biopsies. ESC Heart Fail https://doi.org/10.1002/ehf2.12805.

Ginhoux, F., and Jung, S. (2014). Monocytes and macrophages: developmental pathways and tissue homeostasis. Nat. Rev. Immunol. *14*, 392–404. https://doi.org/10.1038/nri3671.

Gnecchi, M., Moretti, F., Bassi, E.M., Leonardi, S., Totaro, R., Perotti, L., Zuccaro, V., Perlini, S., Preda, L., Baldanti, F., et al. (2020). Myocarditis in a 16-year-old boy positive for SARS-CoV-2. Lancet *395*, e116. https://doi.org/10.1016/S0140-6736(20)31307-6.

Guo, T., Fan, Y., Chen, M., Wu, X., Zhang, L., He, T., Wang, H., Wan, J., Wang, X., and Lu, Z. (2020). Cardiovascular implications of fatal outcomes of patients with coronavirus disease 2019 (COVID-19). JAMA Cardiol. https://doi.org/10.1001/jamacardio.2020.1017.

Han, Y., Duan, X., Yang, L., Nilsson-Payant, B.E., Wang, P., Duan, F., Tang, X., Yaron, T.M., Zhang, T., Uhl, S., et al. (2021). Identification of SARS-CoV-2 inhibitors using lung and colonic organoids. Nature *589*, 270–275. https://doi.org/10.1038/s41586-020-2901-9.

Hoffmann, M., Kleine-Weber, H., Schroeder, S., Kruger, N., Herrler, T., Erichsen, S., Schiergens, T.S., Herrler, G., Wu, N.H., Nitsche, A., et al. (2020). SARS-CoV-2 cell entry depends on ACE2 and TMPRSS2 and is blocked by a clinically proven protease inhibitor. Cell https://doi.org/10.1016/j.cell.2020.02.052.

Inciardi, R.M., Lupi, L., Zaccone, G., Italia, L., Raffo, M., Tomasoni, D., Cani, D.S., Cerini, M., Farina, D., Gavazzi, E., et al. (2020). Cardiac involvement in a patient with coronavirus disease 2019 (COVID-19). JAMA Cardiol. *5*, 819–824. https://doi.org/10.1001/jamacardio.2020.1096.

Jiang, R.D., Liu, M.Q., Chen, Y., Shan, C., Zhou, Y.W., Shen, X.R., Li, Q., Zhang, L., Zhu, Y., Si, H.R., et al. (2020). Pathogenesis of SARS-CoV-2 in transgenic mice expressing human angiotensin-converting enzyme 2. Cell https://doi.org/10.1016/j.cell.2020.05.027.

Lindner, D., Fitzek, A., Brauninger, H., Aleshcheva, G., Edler, C., Meissner, K., Scherschel, K., Kirchhof, P., Escher, F., Schultheiss, H.P., et al. (2020). Association of cardiac infection with SARS-CoV-2 in confirmed COVID-19 autopsy cases. JAMA Cardiol. https://doi.org/10.1001/jamacardio.2020.3551.

Marchiano, S., Hsiang, T.-Y., Khanna, A., Higashi, T., Whitmore, L.S., Bargehr, J., Davaapil, H., Chang, J., Smith, E., Ong, L.P., et al. (2021). SARS-CoV-2 infects human pluripotent stem cell-derived cardiomyocytes, impairing electrical and mechanical function. Stem Cell Reports https://doi.org/10.1016/j.stemcr.2021.02.008.

Riphagen, S., Gomez, X., Gonzalez-Martinez, C., Wilkinson, N., and Theocharis, P. (2020). Hyperinflammatory shock in children during COVID-19 pandemic. Lancet https://doi.org/10.1016/S0140-6736(20)31094-1.

Ruan, Q., Yang, K., Wang, W., Jiang, L., and Song, J. (2020). Clinical predictors of mortality due to COVID-19 based on an analysis of data of 150 patients from Wuhan, China. Intensive Care Med. *46*, 846–848. https://doi.org/10.1007/s00134-020-05991-x.

Shang, J., Wan, Y., Luo, C., Ye, G., Geng, Q., Auerbach, A., and Li, F. (2020). Cell entry mechanisms of SARS-CoV-2. Proc. Natl. Acad. Sci. U S A. *117*, 11727–11734. https://doi.org/10.1073/pnas.2003138117.

Sharma, A., Garcia, G., Jr., Wang, Y., Plummer, J.T., Morizono, K., Arumugaswami, V., and Svendsen, C.N. (2020). Human iPSC-derived cardiomyocytes are susceptible to SARS-CoV-2 infection. Cell Rep Med *1*, 100052. https://doi.org/10.1016/j.xcrm.2020.100052.

Shi, S., Qin, M., Shen, B., Cai, Y., Liu, T., Yang, F., Gong, W., Liu, X., Liang, J., Zhao, Q., et al. (2020). Association of cardiac injury with mortality in hospitalized patients with COVID-19 in Wuhan, China. JAMA Cardiol. https://doi.org/10.1001/jamacardio.2020.0950.

Tavazzi, G., Pellegrini, C., Maurelli, M., Belliato, M., Sciutti, F., Bottazzi, A., Sepe, P.A., Resasco, T., Camporotondo, R., Bruno, R., et al. (2020). Myocardial localization of coronavirus in COVID-19 cardiogenic shock. Eur. J. Heart Fail *22*, 911–915. https://doi.org/10.1002/ejhf.1828.

Tsai, S.Y., Ghazizadeh, Z., Wang, H.J., Amin, S., Ortega, F.A., Badieyan, Z.S., Hsu, Z.T., Gordillo, M., Kumar, R., Christini, D.J., et al. (2020). A human embryonic stem cell reporter line for monitoring chemical-induced cardiotoxicity. Cardiovasc. Res. *116*, 658–670. https://doi.org/10.1093/cvr/cvz148.

Vallania, F., Tam, A., Lofgren, S., Schaffert, S., Azad, T.D., Bongen, E., Haynes, W., Alsup, M., Alonso, M., Davis, M., et al. (2018). Leveraging heterogeneity across multiple datasets increases cell-mixture deconvolution accuracy and reduces biological and technical biases. Nat. Commun. *9*, 4735. https://doi.org/10.1038/s41467-018-07242-6.

Wang, D., Hu, B., Hu, C., Zhu, F., Liu, X., Zhang, J., Wang, B., Xiang, H., Cheng, Z., Xiong, Y., et al. (2020). Clinical characteristics of 138 hospitalized patients with 2019 novel coronavirus-infected pneumonia in Wuhan, China. JAMA https://doi.org/10.1001/jama.2020.1585.

Yang, L., Han, Y., Nilsson-Payant, B.E., Gupta, V., Wang, P., Duan, X., Tang, X., Zhu, J., Zhao, Z., Jaffre, F., et al. (2020). A human pluripotent stem cell-based platform to study SARS-CoV-2 tropism and model virus infection in human cells and organoids. Cell Stem Cell *27*, 125–136.e7. https://doi.org/10.1016/j.stem.2020.06.015.

Yao, X.H., Li, T.Y., He, Z.C., Ping, Y.F., Liu, H.W., Yu, S.C., Mou, H.M., Wang, L.H., Zhang, H.R., Fu, W.J., et al. (2020). A pathological report of three COVID-19 cases by minimally invasive autopsies. Zhonghua Bing Li Xue Za Zhi *49*, E009. https://doi.org/10.3760/cma.j.cn112151-20200312-00193.

Yiangou, L., Davis, R.P., and Mummery, C.L. (2021). Using cardiovascular cells from human pluripotent stem cells for COVID-19 research: why the heart fails. Stem Cell Reports *16*, 385–397. https://doi.org/10.1016/j.stemcr.2020.11.003.

Zhou, F., Yu, T., Du, R., Fan, G., Liu, Y., Liu, Z., Xiang, J., Wang, Y., Song, B., Gu, X., et al. (2020). Clinical course and risk factors for mortality of adult inpatients with COVID-19 in Wuhan, China: a retrospective cohort study. Lancet *395*, 1054–1062. https://doi.org/10.1016/S0140-6736(20)30566-3.

Stem Cell Reports, Volume *16*

Supplemental Information

Cardiomyocytes recruit monocytes upon SARS-CoV-2 infection by secreting CCL2

Liuliu Yang, Benjamin E. Nilsson-Payant, Yuling Han, Fabrice Jaffré, Jiajun Zhu, Pengfei Wang, Tuo Zhang, David Redmond, Sean Houghton, Rasmus Møller, Daisy Hoagland, Lucia Carrau, Shu Horiuchi, Marisa Goff, Jean K. Lim, Yaron Bram, Chanel Richardson, Vasuretha Chandar, Alain Borczuk, Yaoxing Huang, Jenny Xiang, David D. Ho, Robert E. Schwartz, Benjamin R. tenOever, Todd Evans, and Shuibing Chen

SUPPLEMENTAL INFORMATION

Figure S1

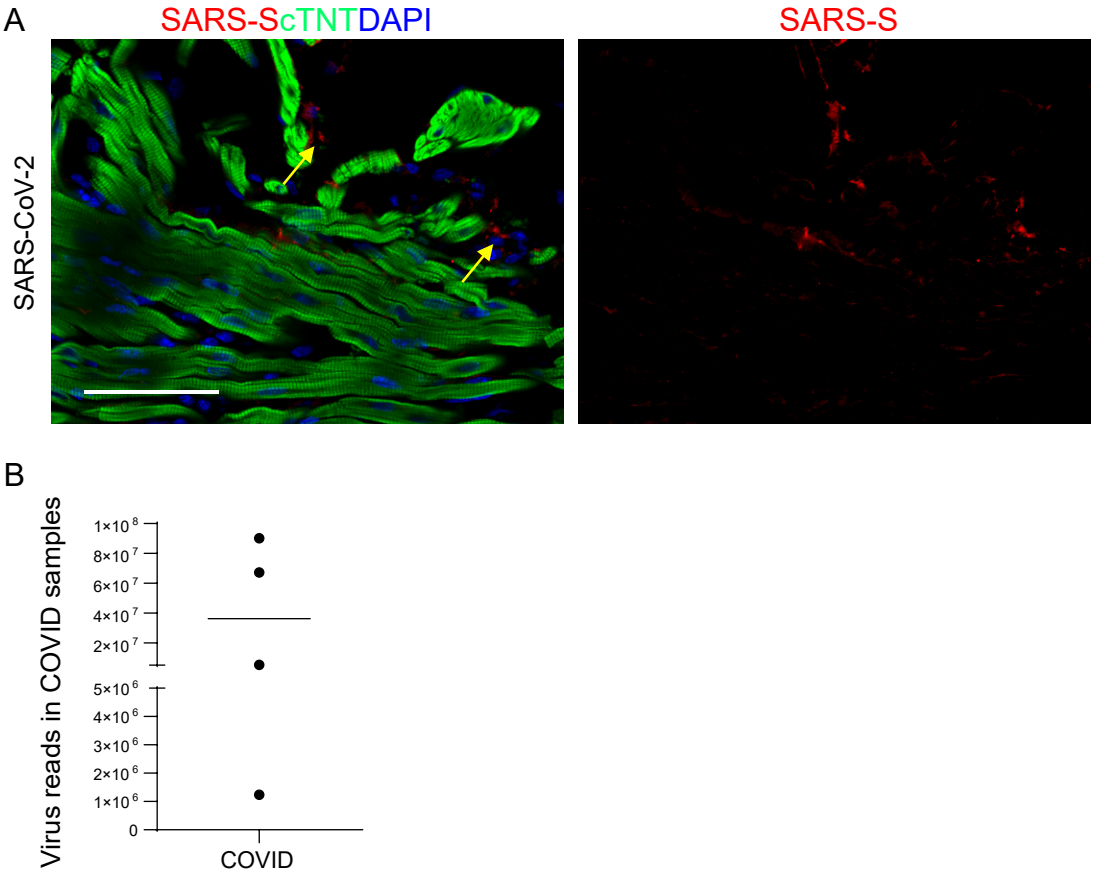
A
SARS-ScTNTDAPI
SARS-S
SARS-CoV-2
B
Virus reads in COVID samples
1×10 8
8×10 7
6×10 7
4×10 7
2×10 7
5×10 6
4×10 6
3×10 6
2×10 6
1×10 6
0
COVID

Supplemental Figure Legends

Figure S1. SARS-S staining in infected hamster heart tissue and viral reads in human COVID-19 heart samples, related to Figure 1.

(A) Immunofluorescences staining shows and example of SARS-S signal in non-CMs. Scale bar=50 μm.

(B) Total virus RNA-seq reads in human COVID-19 samples (N=4 COVID-19 patients).

Figure S2

A

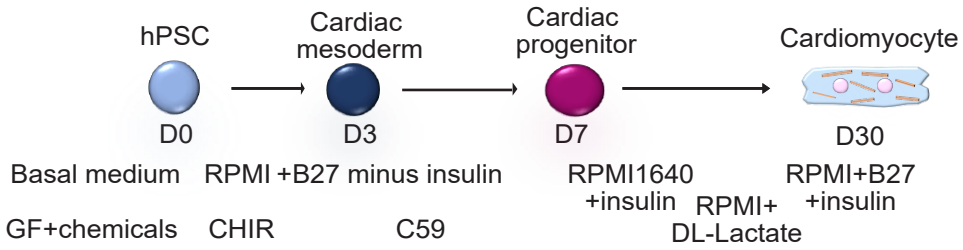
hPSC
Cardiac mesoderm
Cardiac progenitor
Cardiomyocyte
D0
D3
D7
D30
Basal medium
RPMI +B27 minus insulin
RPMI1640 +insulin
RPMI+B27 +insulin
GF+chemicals
CHIR
C59
RPMI+ DL-Lactate

B

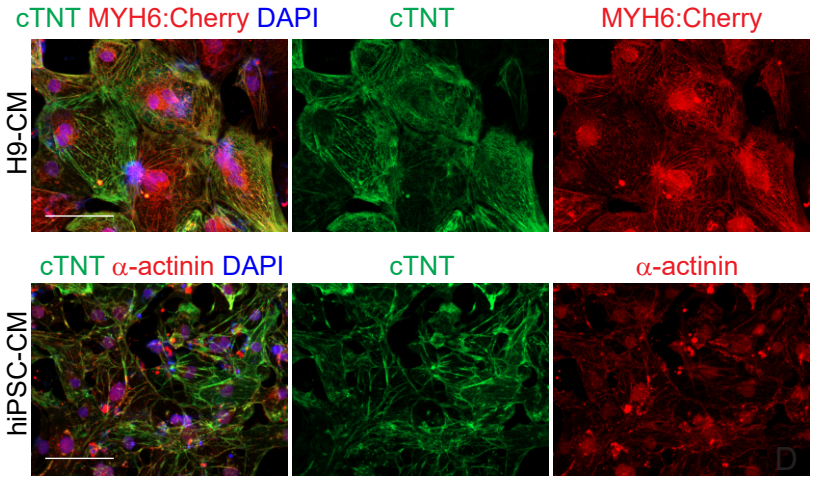
cTNT MYH6:Cherry DAPI
cTNT
MYH6:Cherry
H9-CM
cTNT α-actinin DAPI
cTNT
α-actinin
hiPSC-CM

Figure S2. Stepwise differentiation of hPSCs toward CMs, related to Figure 3.

(A) Scheme of stepwise differentiation of hPSCs toward CMs.

(B) Immunostaining of the hPSC-derived CMs. Scale bar= 100 μm.

Figure S3

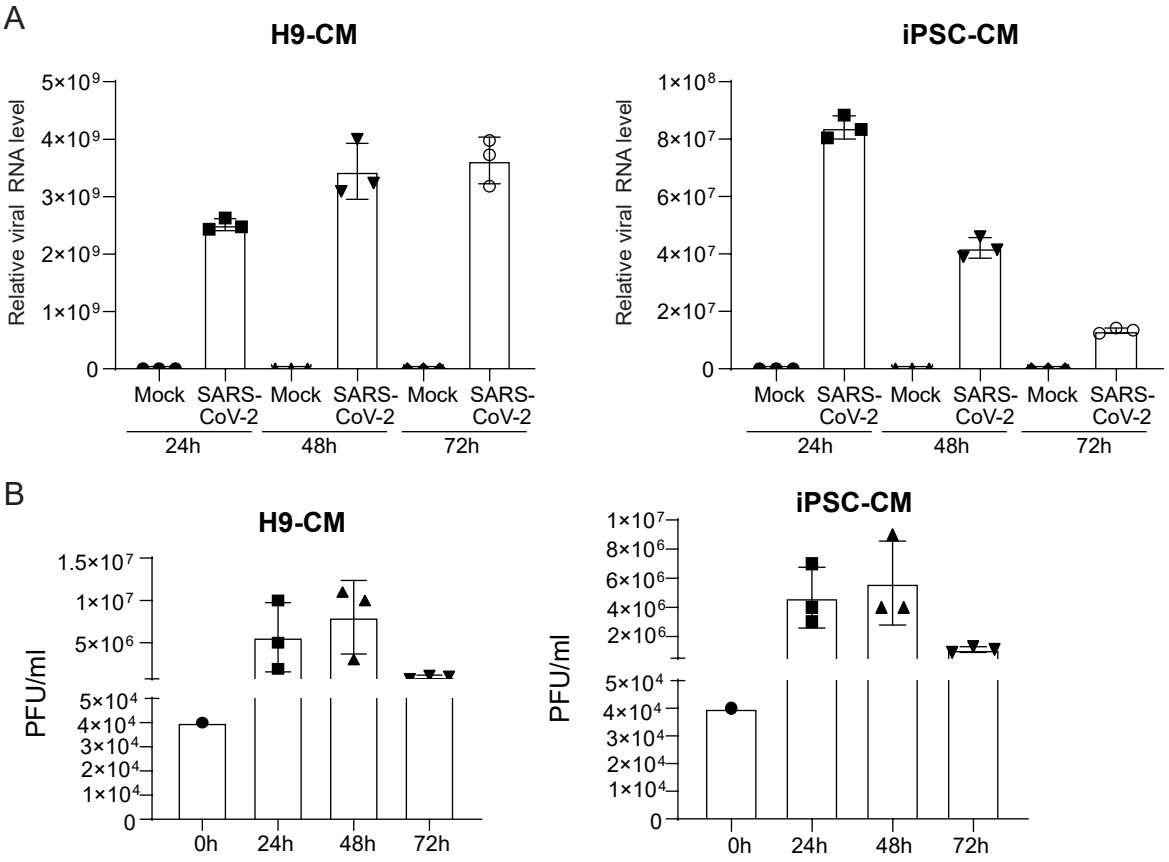
A
H9-CM
iPSC-CM
Relative viral RNA level
5×10⁹
4×10⁹
3×10⁹
2×10⁹
1×10⁹
0
1×10⁸
8×10⁷
6×10⁷
4×10⁷
2×10⁷
Mock
SARS-CoV-2
24h
48h
72h
B
H9-CM
iPSC-CM
PFU/ml
1.5×10⁷
1×10⁷
5×10⁶
5×10⁴
4×10⁴
3×10⁴
2×10⁴
1×10⁴
1×10⁷
8×10⁶
6×10⁶
4×10⁶
2×10⁶
0h
24h
48h
72h

Figure S3. Time course experiment to monitor the SARS-CoV-2 infection on hESC-derived and iPSC-derived CMs, related to Figure 3.

(A) Relative viral RNA expression levels in mock or SARS-CoV-2 (MOI=0.1) infected H9-derived CMs or iPSC-derived CMs at 24, 48, 72 hpi.

(B) Plaque assay of mock or SARS-CoV-2 (MOI=0.1) infected H9-derived CMs or iPSC-derived CMs at 0, 24, 48, 72 hpi. Red lines indicate the input virus (0h indicates the input virus: $4x10^4$ Pfu).

N=3 independent biological replicates. Data was presented as mean ± STDEV.

Figure S4

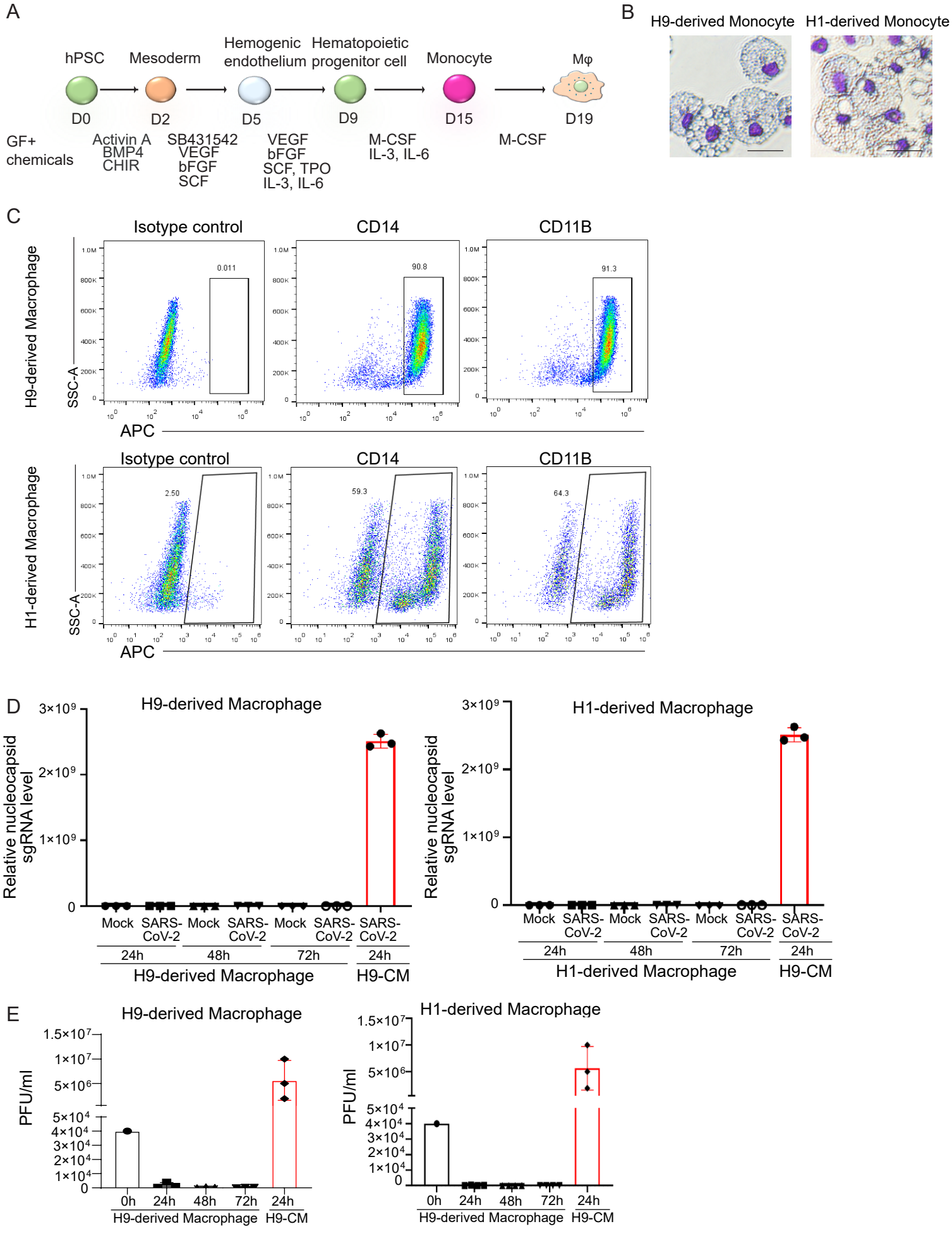
A
hPSC
Mesoderm
Hemogenic endothelium
Hematopoietic progenitor cell
Monocyte
Mφ
D0
D2
D5
D9
D15
D19
GF+ chemicals
Activin A BMP4 CHIR
SB431542 VEGF bFGF SCF
VEGF bFGF SCF, TPO IL-3, IL-6
M-CSF IL-3, IL-6
M-CSF
B
H9-derived Monocyte
H1-derived Monocyte
C
Isotype control
CD14
CD11B
H9-derived Macrophage
H1-derived Macrophage
SSC-A
APC
0.011
90.8
91.3
2.50
59.3
64.3
D
H9-derived Macrophage
H1-derived Macrophage
Relative nucleocapsid sgRNA level
Mock
SARS-CoV-2
24h
48h
72h
H9-derived Macrophage
H9-CM
E
H9-derived Macrophage
H1-derived Macrophage
PFU/ml
0h
24h
48h
72h
H9-derived Macrophage
H9-CM

Figure S4. Stepwise differentiation of hPSCs toward macrophages, related to Figure 6.

(A) Scheme of stepwise differentiation of hPSCs toward macrophages.

(B) Swiss-Giemsa staining of hPSC-derived monocytes. Scale bar= 25 μm.

(C) FACS analysis of hPSC-derived macrophages using CD14 and CD11B antibodies.

(D) Relative viral RNA expression levels in mock or SARS-CoV-2 (MOI=0.1) infected H9-derived macrophages or H1-derived macrophages at 24, 48, 72 hpi. Relative viral RNA expression in SARS-CoV-2 infected CMs at 24 hpi was included as a positive control.

(E) Plaque assay of mock or SARS-CoV-2 (MOI=0.1) infected H9-derived macrophages or H1-derived macrophages at 0, 24, 48, 72 hpi. Plaque numbers of SARS-CoV-2 infected CMs at 24 hpi was included as a positive control. (0h indicates the input virus: $4x10^4$ Pfu).

N=3 independent biological replicates. Data was presented as mean ± STDEV.

Figure S5

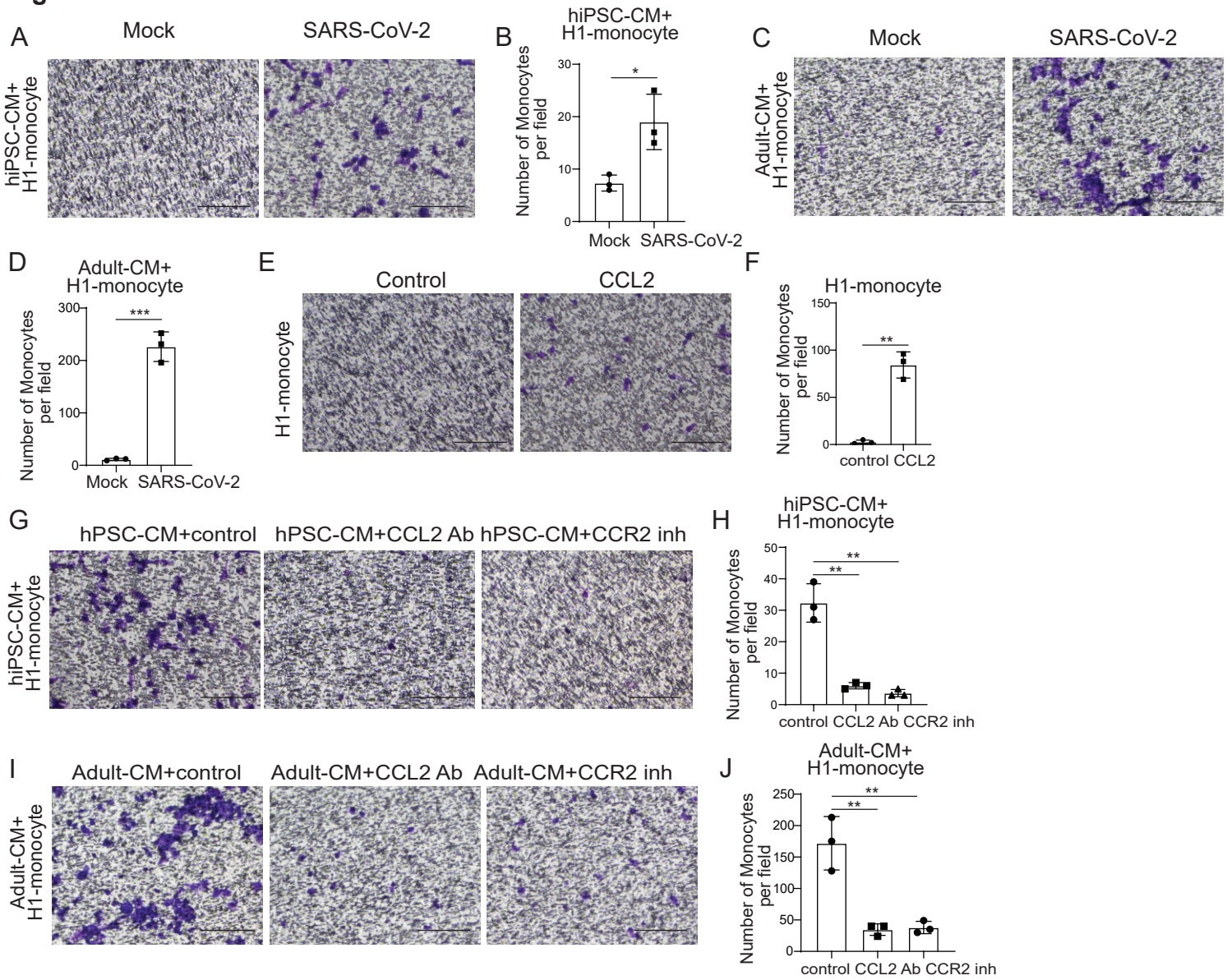
A
Mock
SARS-CoV-2
hiPSC-CM+ H1-monocyte
B
hiPSC-CM+ H1-monocyte
Number of Monocytes per field
Mock
SARS-CoV-2
C
Mock
SARS-CoV-2
Adult-CM+ H1-monocyte
D
Adult-CM+ H1-monocyte
Number of Monocytes per field
Mock
SARS-CoV-2
E
Control
CCL2
H1-monocyte
F
H1-monocyte
Number of Monocytes per field
control
CCL2
G
hPSC-CM+control
hPSC-CM+CCL2 Ab
hPSC-CM+CCR2 inh
hiPSC-CM+ H1-monocyte
H
hiPSC-CM+ H1-monocyte
Number of Monocytes per field
control
CCL2 Ab
CCR2 inh
I
Adult-CM+control
Adult-CM+CCL2 Ab
Adult-CM+CCR2 inh
Adult-CM+ H1-monocyte
J
Adult-CM+ H1-monocyte
Number of Monocytes per field
control
CCL2 Ab
CCR2 inh

Figure S5. CMs recruit monocytes following SARS-CoV-2 infection through secreting CCL2, related to Figure 6.

(A and B) Phase contract images (A) and quantification (B) of migrated H1-derived monocytes recruited by hiPSC-derived CMs infected with SARS-CoV-2 virus or mock-infected in the monocyte migration assay. Scale bar= 100 μm.

(C and D) Phase contract images (C) and quantification (D) of H1-derived monocytes recruited by adult human CMs infected with SARS-CoV-2 virus or mock-infected in the monocyte recruitment assay. Scale bar= 100 μm.

(E and F) Phase contrast images (E) and quantification (F) of migrated H1-derived monocytes by CCL2 in the monocyte recruitment assay. Scale bar= 100 μm.

(G and H) Phase contrast images (G) and quantification (H) of migrated H1-derived monocytes recruited by hiPSC-derived CMs infected with SARS-CoV-2 virus and treated with CCL2 neutralizing antibody or CCR2 inhibitor (RS504393) in the monocyte recruitment assay. Scale bar= 100 μm.

(I and J) Phase contrast images (I) and quantification (J) of migrated H1-derived monocytes recruited by adult human CMs infected with SARS-CoV-2 virus and treated with CCL2 neutralizing antibody or CCR2 inhibitor in the monocyte recruitment assay. Scale bar= 100 μm.

N=3 independent biological replicates. Data was presented as mean ± STDEV. *P* values were calculated by unpaired two-tailed Student's t test. **P* < 0.05, ***P* < 0.01, and ****P* < 0.001.

Figure S6

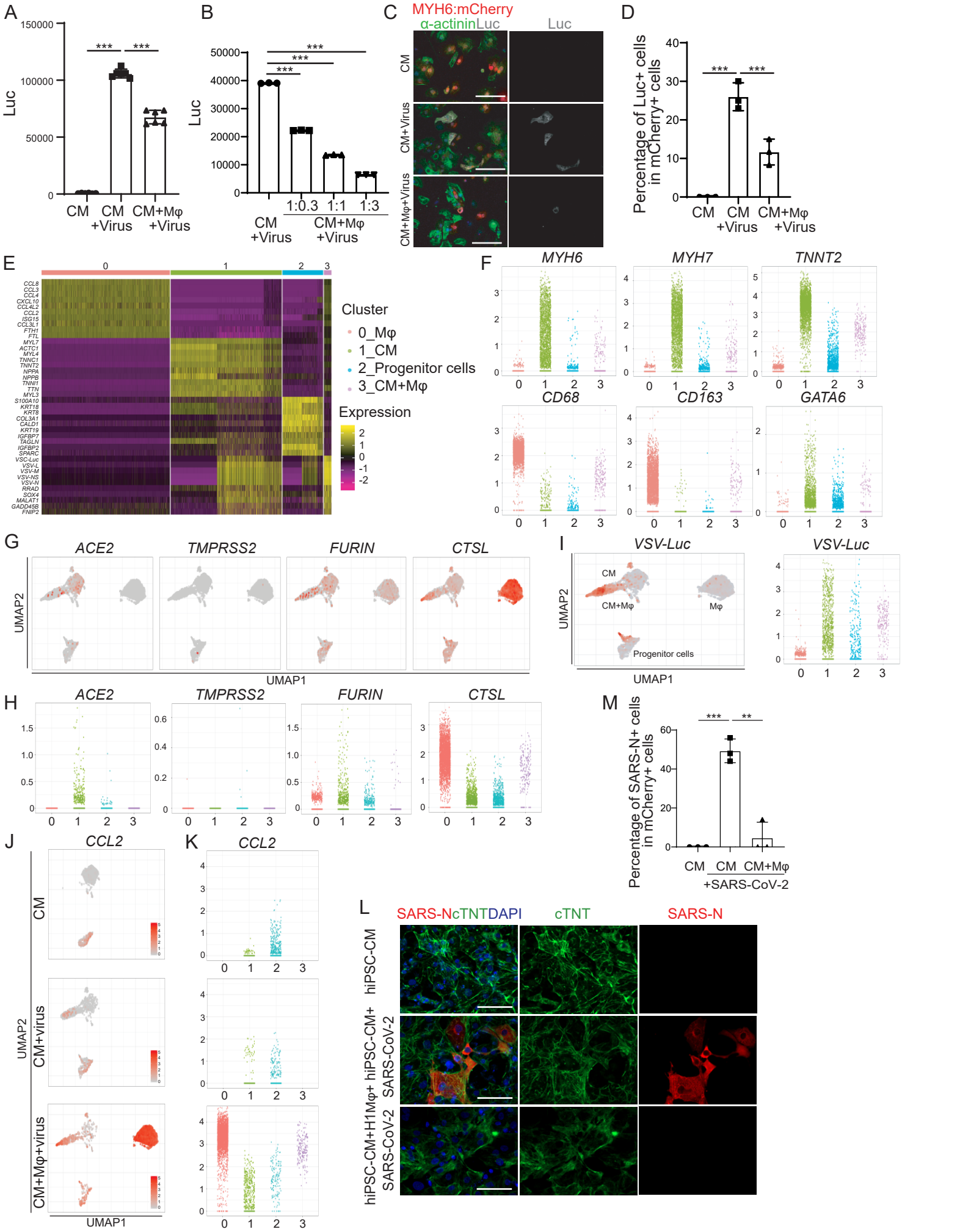
A
Luc
150000
100000
50000
0
***
***
CM
CM +Virus
CM+Mφ +Virus
B
Luc
50000
40000
30000
20000
10000
0
***
***
***
1:0.3
1:1
1:3
CM +Virus
CM+Mφ +Virus
C
MYH6:mCherry
α-actininLuc
Luc
CM
CM+Virus
CM+Mφ+Virus
D
Percentage of Luc+ cells in mCherry+ cells
40
30
20
10
0
***
***
CM
CM +Virus
CM+Mφ +Virus
E
0
1
2
3
CCL8
CCL3
CCL4
CXCL10
CCL4L2
CCL2
ISG15
CCL3L1
FTH1
FTL
MYL7
ACTC1
MYL4
TNNC1
TNNT2
NPPA
NPPB
TNNI1
TTN
MYL3
S100A10
KRT18
KRT8
COL3A1
GALD1
KRT19
IGFBP7
TAGLN
IGFBP2
SPARC
VSC-Luc
VSV-L
VSV-M
VSV-NS
VSV-N
RRAD
SOX4
MALAT1
GADD45B
FNIP2
Cluster
0_Mφ
1_CM
2_Progenitor cells
3_CM+Mφ
Expression
2
1
0
-1
-2
F
MYH6
MYH7
TNNT2
CD68
CD163
GATA6
G
ACE2
TMPRSS2
FURIN
CTSL
UMAP2
UMAP1
I
VSV-Luc
CM
CM+Mφ
Mφ
Progenitor cells
UMAP2
UMAP1
VSV-Luc
H
ACE2
TMPRSS2
FURIN
CTSL
M
Percentage of SARS-N+ cells in mCherry+ cells
60
40
20
0
***
**
CM
CM +SARS-CoV-2
CM+Mφ +SARS-CoV-2
J
CCL2
UMAP2
CM
CM+virus
CM+Mφ+virus
UMAP1
K
CCL2
L
SARS-NcTNTDAPI
cTNT
SARS-N
hiPSC-CM
hiPSC-CM+ SARS-CoV-2
hiPSC-CM+Mφ+ SARS-CoV-2

Figure S6. Single cell RNA-seq analysis of immunocardiac co-cultured cells upon SARS-CoV-2-entry virus infection, related to Figure 7.

(A) Luciferase activity at 24 hpi of hPSC-derived CMs mock-infected or infected with SARS-CoV-2-entry virus in the presence or absence of macrophages (MOI=0.1).

(B) Luciferase activity at 24 hpi of H9-derived CMs infected with SARS-CoV-2-entry virus and co-cultured with different ratio of macrophages (MOI=0.1).

(C and D) Immunostaining (**C**) and quantification (**D**) of Luc in hPSC-derived CMs at 24 hpi mock-infected or infected with SARS-CoV-2-entry virus in the presence or absence of macrophages (MOI=0.1).

(E) Heatmap of enriched genes in each cluster of scRNA profiles of the immunocardiac co-culture platform containing hPSC-derived CMs and macrophages upon SARS-CoV-2-entry virus infection.

(F) Jitter plot of cell type specific markers in the immunocardiac co-culture platform containing hPSC-derived CMs and macrophages upon SARS-CoV-2-entry virus infection.

(G) UMAP of *ACE2*, *TMPRSS2*, *FURIN*, *CTSL* genes in the immunocardiac co-culture platform containing H9-derived CMs and macrophages upon SARS-CoV-2-entry virus infection.

(H) Jitter plot of *ACE2*, *TMPRSS2*, *FURIN*, *CTSL* genes in the immunocardiac co-culture platform containing H9-derived CMs and macrophages upon SARS-CoV-2-entry virus infection.

(I) UMAP and jitter plot of SARS-CoV-2-entry virus gene in the immunocardiac co-culture platform containing hPSC-derived CMs and macrophages upon SARS-CoV-2-entry virus infection.

(J) UMAP analysis of *CCL2* in H9-derived CMs mock-infected (CM) or infected with SARS-CoV-2-entry virus (CM+virus) and the virus-immunocardiac co-culture platform containing H9-derived CMs and H9-derived macrophages infected with SARS-CoV-2-entry virus (CM+macrophage+virus).

(K) Jitter plot of *CCL2* in H9-derived CMs mock-infected (CM) or infected with SARS-CoV-2-entry virus (CM+virus) and the virus-immunocardiac co-culture platform containing H9-derived CMs and H9-derived macrophages infected with SARS-CoV-2-entry virus (CM+macrophage+virus).

(L and M) Immunostaining (L) and quantification (M) of SARS-N^+ cells in $cTNT^+$ hiPSC-derived CMs at 24 hpi mock-infected or infected with SARS-CoV-2 in the presence or absence of H1-derived macrophages (MOI=0.1). Scale bar= 50 μm.

N=3 independent biological replicates. Data was presented as mean ± STDEV. *P* values were calculated by unpaired two-tailed Student's t test. $^{**}P < 0.01$, and $^{***}P < 0.001$.

Figure S7

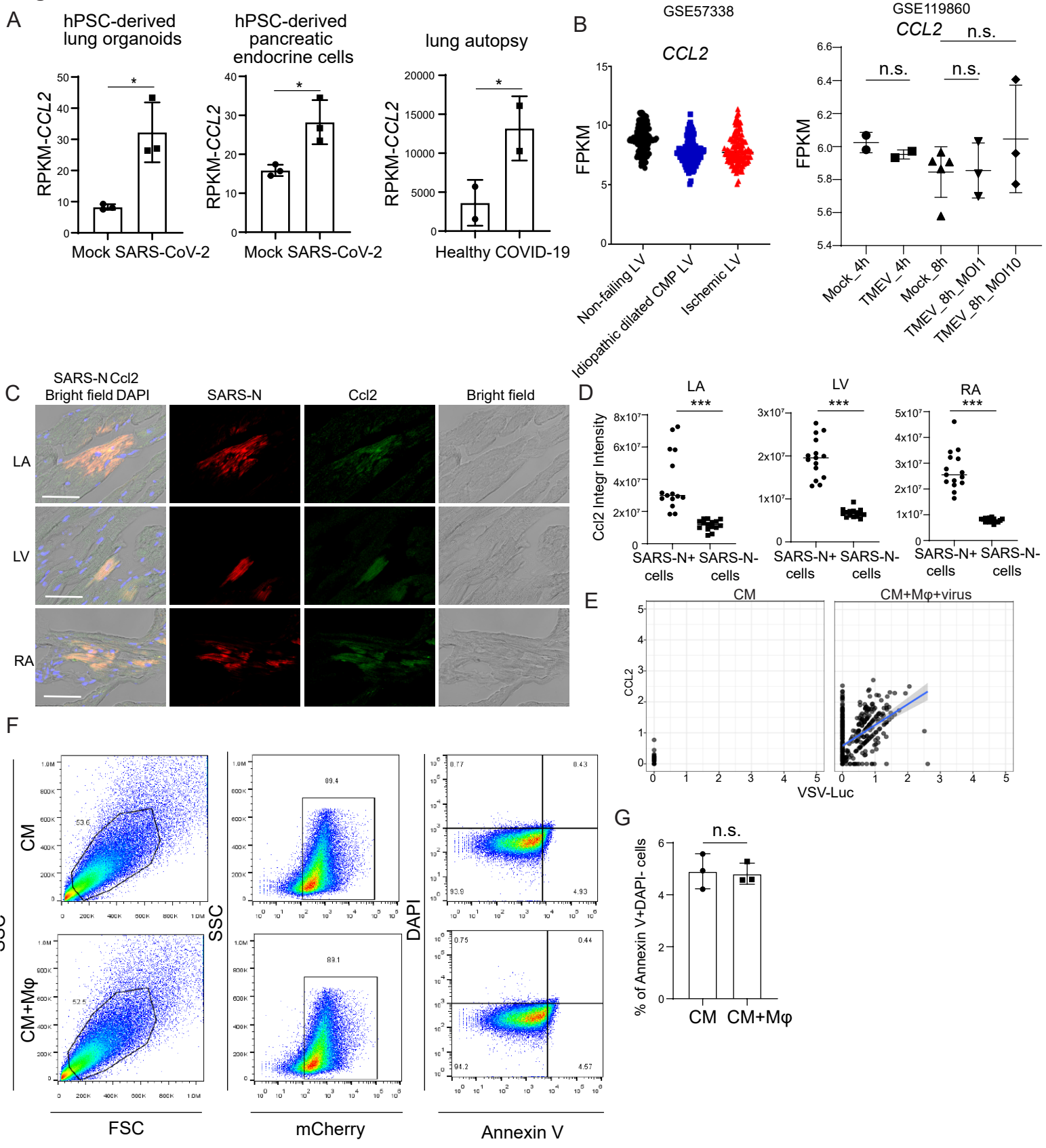
A
hPSC-derived lung organoids
RPKM-CCL2
Mock SARS-CoV-2
hPSC-derived pancreatic endocrine cells
RPKM-CCL2
Mock SARS-CoV-2
lung autopsy
RPKM-CCL2
Healthy COVID-19
B
GSE57338
CCL2
FPKM
Non-failing LV
Idiopathic dilated CMP LV
Ischemic LV
GSE119860
CCL2
n.s.
n.s.
n.s.
FPKM
Mock_4h
TMEV_4h
Mock_8h
TMEV_8h_MOI1
TMEV_8h_MOI10
C
SARS-N Ccl2 Bright field DAPI
SARS-N
Ccl2
Bright field
LA
LV
RA
D
LA
LV
RA
***
Ccl2 Integr Intensity
SARS-N+ cells
SARS-N- cells
E
CM
CM+Mφ+virus
CCL2
VSV-Luc
F
SSC
CM
CM+Mφ
FSC
SSC
mCherry
DAPI
Annexin V
G
n.s.
% of Annexin V+DAPI- cells
CM
CM+Mφ

Figure S7. CCL2 expression in SARS-CoV-2 infected cells and COVID-19 patients, related to Figure 7.

(A) *CCL2* expression levels in mock-infected or SARS-CoV-2 infected hPSC-derived lung organoids (N=3 for mock, N=3 for SARS-CoV-2), hPSC-derived pancreatic endocrine cells (N=3 for mock, N=3 for SARS-CoV-2) and lung autopsy samples of non-COVID-19 (N=2) and COVID-19 patients (N=2).

(B) Left, *CCL2* expression of non-failing LVs, idiopathic dilated cardiomyopathy LVs and ischemic LVs (GSE57338). Right, *CCL2* expression in murine encephalomyelitis virus (TMEV) infected cardiomyocytes or mock infected cardiomyocytes (GSE119860).

(C and D) Immunostaining (C) and quantification (D) of SARS-N and Ccl2 in SARS-CoV-2 infected hamster heart. Scale bar = 50 μm.

(E) Correlation between CCL2 expression and VSV-Luc expression in CM and CM+macrophage+virus groups.

(F and G) Flow cytometry analysis (F) and quantification (G) of apoptotic cells in H9-derived CMs in the presence or absence of H9-derived macrophages using a trans-well assay.

N=3 independent biological replicates. Data was presented as mean ± STDEV. *P* values were calculated by unpaired two-tailed Student's t test. **P* < 0.05, ****P* < 0.001 and n.s., non-significant.

Movie S1. $Ca2^+$ flux intensity of mock infected H9-derived CMs at 48 hpi, related to Figure 3.

Movie S2. $Ca2^+$ flux intensity of SARS-CoV-2 infected H9-derived CMs at 48 hpi, related to Figure 3.

Table S1. Antibodies used for immunocytochemistry and intracellular flow cytometric analysis, related to Figure 1, Figure 2, Figure 3, Figure 5 and Figure 7.

Table S2. Primers used for qRT-PCR, related to Figure 3, Figure 5 and Figure 7.

Primer name	Sequence
ACTB-human-Forward	*CGTCACCAACTGGGACGACA*
ACTB- human-Reverse	*CTTCTCGCGGTTGGCCTTGG*
SARS-CoV-2-TRS-L	*CTCTTGTAGATCTGTTCTCTAAACGAAC*
SARS-CoV-2-TRS-N	*GGTCCACCAAACGTAATGCG*
cTNT-Forward	*TTCACCAAAGATCTGCTCCTCGCT*
cTNT-Reverse	*TTATTACTGGTGTGGAGTGGGTGTGG*
ACTB-hamster-Forward	*CACCATTGGCAACGAGCGGTTC*
ACTB- hamster-Reverse	*AGGTCTTTGCGGATGTCGACGT*
CCL2-hamster-Forward	*CAGCCAGACTCCGTTAACTCC*
CCL2- hamster-Reverse	*TGTATGCCTGGACCCAGTCCT*

EXPERIMENTAL PROCEDURES

Cell lines

Vero E6 (African green monkey [*Chlorocebus aethiops*] kidney) were obtained from ATCC (https://www.atcc.org/). Cells were cultured in Dulbecco's Modified Eagle Medium (DMEM) supplemented with 10% FBS and 100 I.U./mL penicillin and 100 μg/mL streptomycin. All cell lines were incubated at 37°C with 5% CO_2.

Propagation and titration of SARS-CoV-2

SARS-CoV-2, isolate USA-WA1/2020 (NR-52281) was deposited by the Center for Disease Control and Prevention and obtained through BEI Resources, NIAID, NIH. SARS-CoV-2 was propagated in Vero E6 cells in DMEM supplemented with 2% FBS. Virus stocks were filtered and concentrated by centrifugation using Amicon Ultra-15 Centrifugal filter units (100 KDa MWCO). Infectious titers were determined by plaque assays in Vero E6 cells in Minimum Essential Media supplemented with 2% FBS, 4 mM L-glutamine, 0.2% BSA, 10 mM HEPES and 0.12% NaHCO3 and 0.7% OXOID agar as has been described previously(Blanco-Melo et al., 2020). All work involving live SARS-CoV-2 was performed in the CDC/USDA-approved BSL-3 facility of the Global Health and Emerging Pathogens Institute at the Icahn School of Medicine at Mount Sinai in accordance with institutional biosafety requirements.

SARS-CoV-2 infections of hamsters

3-5-week-old male Golden Syrian hamsters (*Mesocricetus auratus*) were obtained from Charles River. Hamsters were acclimated to the CDC/USDA-approved BSL-3 facility of the Global Health and Emerging Pathogens Institute at the Icahn School of Medicine at Mount Sinai for 2-4 days. Before intranasal infection, hamsters were anesthetized by intraperitoneal injection with a ketamine HCl/xylazine solution (4:1). Hamsters were intranasally inoculated with 100 pfu of SARS-CoV-2 in PBS (or PBS only as a control) in a total volume of 100 μl. Two days post-infection hamsters were euthanized and hearts were collected. For hearts analyzed by immunofluorescence staining, hamsters were perfused with 60 ml of ice-cold PBS before tissue collection and collected hearts were immediately placed in 10% nonbuffered formalin (NFB) and fixed for 24 hr. For transcriptomic analysis, collected hearts were placed in TRIzol for further RNA extraction.

SARS-CoV-2 live virus infection

The immunocardiac co-culture containing hPSC-derived CMs and macrophages were infected with SARS-CoV-2 at an MOI of 0.1 and incubated at 37°C for 24 hr. Infected cells were either lysed in TRIzol for RNA analysis or fixed in 5% formaldehyde for 24 hr for immunofluorescence staining, prior to safe removal from the BSL-3 facility.

hPSC-derived cardiomyocyte differentiation

To differentiate cardiomyocytes (CMs) from hPSC, hPSCs were passaged at a density of $3x10^5$cells/well of 6-well plate and grown for 48 hr in a humidified incubator with 5% CO_2 at 37°C to reach 90% confluence. On day 0, the medium was replaced with RPMI 1640 supplemented with B27 minus insulin and 6 μM CHIR99021. On day 2, the medium was changed to RPMI 1640 supplemented with B27 minus insulin for 24 hr. Day 3, medium was refreshed to RPMI 1640 supplemented with B27 minus insulin and 5 μM XAV939 for 48 h. On day 5, the medium was changed back to RPMI-B27 minus insulin for 48 hr, and then switched to RPMI 1640 plus normal B27 until day 12. The medium was changed every other day. On day 12, the medium was transiently

changed to RPMI 1640 without D-glucose containing ascorbic acid, human albumin and DL-Lactate for two days to allow metabolic purification of CMs. From that day on, fresh RPMI 1640 plus normal B27 was changed every two days. On day 21, cells were dissociated with Accutase at 37°C followed by resuspending with fresh RPMI 1640-B27 plus Y-27632 and reseeding into new plates. After 24 hr, medium was switched to RMPI 1640 plus normal B27 without Y-27632 for following experiments. CMs were derived from two hPSC cell lines: H9-MYH6:mCherry ESCs and WT-F5 iPSCs. The protocol details are summarized in Supplemental Figure 2a.

Adult human cardiomyocytes

Adult human cardiomyocytes were purchased from PromoCell (Primary Human Cardiac Myocytes, C-12810) and cultured in Myocyte Growth Medium (PromoCell, C-22070). Cells were incubated at 37°C with 5% CO_2.

hPSC-derived monocytes and macrophage differentiation

Monocytes and macrophages were derived from two hPSC lines: H9 ESCs and H1 ESCs. The differentiation protocol was adapted from a previously reported protocol (Cao et al., 2019). First, hPSC cells were lifted with ReLeSR (STEMCELL Technologies) as small clusters onto Matrigel-coated 6-well plates at a low density. After 1 day, medium was refreshed with IF9S medium supplemented with 50 ng/ml BMP-4, 15 ng/ml Activin A and 1.5 μm CHIR99021. On day 2, medium was refreshed with IF9S medium supplemented with 50 ng/ml VEGF, 50 ng/ml bFGF, 50 ng/ml SCF (R&D Systems) and 10 μm SB431542 (Cayman Chemical). On day 5 and day7, medium was changed into IF9S supplemented with 50 ng/ml IL-6 (R&D Systems), 12 ng/ml IL-3 (R&D Systems), 50 ng/ml VEGF, 50 ng/ml bFGF, 50 ng/ml SCF and 50 ng/ml TPO (R&D Systems). On day 9, cells were dissociated with TrypLE (Life Technologies) and resuspended in IF9S medium supplemented with 50 ng/ml IL-6, 12 ng/ml IL-3 and 80 ng/ml M-CSF (R&D Systems) into low attachment plates. On day 13 and day 15, medium was changed into IF9S supplemented with 50 ng/ml IL-6, 12 ng/ml IL-3 and 80 ng/ml M-CSF. Monocytes could be collected on day 15. For macrophage differentiation, monocytes were plated onto FBS-coated plates with IF9S medium supplemented with 80ng/ml M-CSF. All differentiation steps were cultured under normoxic conditions at 37 °C, 5% CO_2. The protocol details are summarized in Supplemental Fig. 4A.

Monocyte migration assay

The migration of macrophages was examined using 24 well Trans-well chambers (6.5 mm insert; 3.0 μm polycarbonate membrane). The upper well was coated with Matrigel before seeding with macrophages ($2X10^4$ cells). After 24 hr, the chamber was fixed and stained with crystal violet. Migrated cells were counted under an inverted light microscope.

Immunocardiac co-culture

hPSC-derived cardiomyocytes were dissociated with Accutase for 5-10 min at 37°C followed by resuspending with fresh RPMI 1640 plus normal B27 and Y-27632 and reseeding into plates. After 24 hr recovery, the medium was switched to RMPI 1640 plus B27 without Y-27632. After another 24 hr recovery, hPSC-derived macrophages were dissociated with Accutase for 3 min and added into hPSC-derived cardiomyocytes. The immunocardiac co-culture cells were cultured for another 24 hr (short-term co-culture) or 7 days (long-term co-culture) before following analysis. Adult

cardiomyocytes were also seeded into plates for 48-96 hr and co-cultured with hPSC-derived macrophages for another 24 hr before following analysis.

SARS-CoV-2 pseudovirus virus infection

To perform pseudovirus infections, cells were seeded into 96 well plates. Spike pseudo-typed virus(Han et al., 2021) was added at the indicated MOI=0.01. At 2 hpi, infection media was replaced with fresh media. At 24 hpi, cells were harvested and luciferase activity was measured using the Luciferase Assay System protocol (E1501, Promega) or immunostaining analysis.

Immunostaining

Hamster heart tissues were obtained from mock or SARS-CoV-2 infected hamsters. Heart tissues were fixed overnight in 5% formaldehyde, soaked in 30% sucrose and embedded in OCT (Fisher Scientific, Pittsburgh, PA). The slices were wash with PBS 2 times to remove OCT and incubated in 0.1% Triton for 1hr at room temperature. Then, slices were stained with primary antibodies at 4°C overnight and secondary antibodies at RT for 1 hr. The information for primary antibodies and secondary antibodies is provided in Table S1. Nuclei were counterstained by DAPI.

qRT-PCR

Total RNA samples were prepared from tissues or cells using TRIzol and Direct-zol RNA Miniprep Plus kit (Zymo Research) according to the manufacturer's instructions. To quantify viral replication, measured by the expression of sgRNA transcription of the viral N gene, one-step quantitative real-time PCR was performed using SuperScript III Platinum SYBR Green One-Step qRT-PCR Kit (Invitrogen) with primers specific for the TRS-L and TRS-B sites of the *N* gene as well as *ACTB* or *cTNT* as an internal reference. Quantitative real-time PCR reactions were performed on a LightCycler 480 Instrument II (Roche). Delta-delta-cycle threshold (ΔΔCT) was determined relative to the *ACTB* or *cTNT* and mock infected /treated samples. Error bars indicate the standard deviation of the mean from three biological replicates. The sequences of primers/probes are provided in Table S2.

ELISA

CCL2 levels in the supernatant of infected hPSC-derived CMs were evaluated using ELISA. The antibody and cytokine standards were purchased as antibody pairs from R&D Systems (Minneapolis, Minnesota) or Peprotech (Rocky Hill, New Jersey). Individual magnetic Luminex bead sets (Luminex Corp, CA) were coupled to cytokine-specific capture antibodies according to the manufacturer's recommendations. The assays were read on a MAGPIX platform. The median fluorescence intensity of these beads was recorded for each bead and was used for analysis using a custom R script and a 5P regression algorithm.

Sequencing and gene expression UMI counts matrix generation

The 10X libraries were sequenced on the Illumina NovaSeq6000 sequencer with pair-end reads (28 bp for read 1 and 91 bp for read 2). The sequencing data were primarily analyzed by the 10X cellranger pipeline (v3.0.2) in two steps. In the first step, cellranger *mkfastq* demultiplexed samples and generated fastq files; and in the second step, cellranger count aligned fastq files to the reference genome and extracted gene expression UMI counts matrix. In order to measure viral gene expression, we built a custom reference genome by integrating the four virus genes, luciferase and two

fluoresence genes into the 10X pre-built human reference (GRCh38 v3.0.0) using cellranger *mkref*. The sequences of four viral genes (VSV-N, VSV-NS, VSV-M and VSV-L) were retrieved from NCBI (https://www.ncbi.nlm.nih.gov/nuccore/335873), the sequence of the luciferase was retrieved from HIV-Luc, and the sequences of the two fluorescence genes were downloaded from NCBI (mCherry: https://www.ncbi.nlm.nih.gov/nuccore/AY678264.1; GFP: https://www.ncbi.nlm.nih.gov/nuccore/U55761.1).

Single-cell RNA-seq data analysis

We filtered out a small fraction of cells with viral gene content greater than 80% but less than 200 genes detected for which we believe are not real cells but rather empty beads with ambient RNAs. We then filtered out cells with less than 400 or more than 7000 genes detected as well as cells with mitochondria gene content greater than 15%, and used the remaining cells (1654 cells for CM; 1555 cells for CM+virus; 4001 cells for CM+macrophage+virus) for downstream analysis. We normalized the gene expression UMI counts using a deconvolution strategy implemented by the R scran package (v.1.14.1). In particular, we pre-clustered cells using the *quickCluster* function; we computed size factor per cell within each cluster and rescaled the size factors by normalization between clusters using the *computeSumFactors* function; and we normalized the UMI counts per cell by the size factors and took a logarithm transform using the *normalize* function. We further normalized the UMI counts across samples using the *multiBatchNorm* function in the R batchelor package (v1.2.1). We identified highly variable genes using the *FindVariableFeatures* function in the R Seurat package (v3.1.0) (Stuart et al., 2019), and selected the top 3000 variable genes after excluding mitochondria genes, ribosomal genes, dissociation-related genes, viral genes and fluorescence genes. The list of dissociation-related genes was originally built on mouse data (van den Brink et al., 2017); we converted them to human ortholog genes using Ensembl BioMart. We aligned the two samples based on their mutual nearest neighbors (MNNs) using the *fastMNN* function in the R batchelor package, this was done by performing a principal component analysis (PCA) on the highly variable genes and then correcting the principal components (PCs) according to their MNNs. We selected the corrected top 50 PCs for downstream visualization and clustering analysis. We ran UMAP dimensional reduction using the *RunUMAP* function in the R Seurat package with the number of neighboring points setting to 35 and training epochs setting to 2000. We clustered cells into fifteen clusters by constructing a shared nearest neighbor graph and then grouping cells of similar transcriptome profiles using the *FindNeighbors* function and *FindClusters* function (resolution set to 0.7) in the R Seurat package. We identified marker genes for each cluster by performing differential expression analysis between cells inside and outside that cluster using the *FindMarkers* function in the R Seurat package. After reviewing the clusters, we merged them into four clusters representing macrophages, CM, CM+macrophages and progenitor cells, for further analysis. We re-identified marker genes for the merged four clusters and selected top 10 positive marker genes per cluster for heatmap plot using the *DoHeatmap* function in the R Seurat package. The rest plots were generated using the R ggplot2 package.

RNA-Seq

Total RNA was extracted in TRIzol (Invitrogen) and DNase I treated using the Directzol RNA Miniprep kit (Zymo Research) according to the manufacturer's instructions. RNA from hamster hearts was homogenized in TRIzol before RNA extraction. RNA-seq libraries of polyadenylated RNA were prepared using TruSeq

Stranded mRNA Library Prep Kit (Illumina) according to the manufacturer's instructions. cDNA libraries were sequenced on an Illumina NextSeq 500 platform. The sequencing reads were cleaned by trimming adapter sequences and low quality bases using cutadapt v1.9.1 (Kechin et al., 2017), and were aligned to the human reference genome (GRCh37) or the SARS-CoV-2 genome (NC_045512.2) using STAR v2.5.2b (Dobin et al., 2013). Sequencing reads from hamster samples were aligned to a hamster reference genome (downloaded from Ensembl, accession#: GCA 000349665) using HISAT2 2.1.0. Raw gene counts were quantified using HTSeq-count v0.11.2 (Anders et al., 2015). Differential expression analysis was performed using DESeq2 v1.22.2 (Love et al., 2014). Regularized log transformation was applied to convert count data to log2 scale. Sample-to-sample distance matrix was calculated based on the transformed log-scaled count data using R *dist* function. Multidimensional scaling (MDS) was performed on the distance matrix using R *cmdscale* function. PCA plot was drawn using R functions prcomp.

Intracellular flow cytometry analysis

Flow cytometry staining was performed to examine the expression of CD14 and CD11B. Briefly, cells were dissociated with Accutase, then washed twice with PBS containing 0.5% BSA and 2mM EDTA. Incubation with antibody was at 4°C for 1 hr in the dark, following by washing twice and flow cytometry analysis. The information for primary antibodies and secondary antibodies is provided in Table S1.

Human studies

For RNA analysis, tissues were acquired by autopsies from deceased COVID-19 human subjects and processed using TRIzol. Tissue samples were provided by the Weill Cornell Medicine Department of Pathology. The uninfected human heart samples were similarly obtained from non-COVID-19 donors. The Tissue Procurement Facility operates under Institutional Review Board (IRB) approved protocol and follows guidelines set by HIPAA. Experiments using samples from human subjects were conducted in accordance with local regulations and with the approval of the institutional review board at the Weill Cornell Medicine under protocol 20-04021814.

Quantification and Statistical analysis

N=3 independent biological replicates were used for all experiments unless otherwise indicated. n.s. indicates a non-significant difference. *P*-values were calculated by unpaired two-tailed Student's t-test unless otherwise indicated. *$p<0.05$, **$p<0.01$ and ***$p<0.001$.

Reference

Anders, S., Pyl, P.T., and Huber, W. (2015). HTSeq--a Python framework to work with high-throughput sequencing data. Bioinformatics *31*, 166-169. 10.1093/bioinformatics/btu638.

Blanco-Melo, D., Nilsson-Payant, B.E., Liu, W.C., Uhl, S., Hoagland, D., Moller, R., Jordan, T.X., Oishi, K., Panis, M., Sachs, D., et al. (2020). Imbalanced Host Response to SARS-CoV-2 Drives Development of COVID-19. Cell. 10.1016/j.cell.2020.04.026.

Cao, X., Yakala, G.K., van den Hil, F.E., Cochrane, A., Mummery, C.L., and Orlova, V.V. (2019). Differentiation and Functional Comparison of Monocytes and Macrophages from hiPSCs with Peripheral Blood Derivatives. Stem Cell Reports *12*, 1282-1297. 10.1016/j.stemcr.2019.05.003.

Dobin, A., Davis, C.A., Schlesinger, F., Drenkow, J., Zaleski, C., Jha, S., Batut, P., Chaisson, M., and Gingeras, T.R. (2013). STAR: ultrafast universal RNA-seq aligner. Bioinformatics *29*, 15-21. 10.1093/bioinformatics/bts635.

Han, Y., Duan, X., Yang, L., Nilsson-Payant, B.E., Wang, P., Duan, F., Tang, X., Yaron, T.M., Zhang, T., Uhl, S., et al. (2021). Identification of SARS-CoV-2 inhibitors using lung and colonic organoids. Nature *589*, 270-275. 10.1038/s41586-020-2901-9.

Kechin, A., Boyarskikh, U., Kel, A., and Filipenko, M. (2017). cutPrimers: A New Tool for Accurate Cutting of Primers from Reads of Targeted Next Generation Sequencing. J Comput Biol *24*, 1138-1143. 10.1089/cmb.2017.0096.

Love, M.I., Huber, W., and Anders, S. (2014). Moderated estimation of fold change and dispersion for RNA-seq data with DESeq2. Genome Biol *15*, 550. 10.1186/s13059-014-0550-8.

Stuart, T., Butler, A., Hoffman, P., Hafemeister, C., Papalexi, E., Mauck, W.M., 3rd, Hao, Y., Stoeckius, M., Smibert, P., and Satija, R. (2019). Comprehensive Integration of Single-Cell Data. Cell *177*, 1888-1902 e1821. 10.1016/j.cell.2019.05.031.

van den Brink, S.C., Sage, F., Vertesy, A., Spanjaard, B., Peterson-Maduro, J., Baron, C.S., Robin, C., and van Oudenaarden, A. (2017). Single-cell sequencing reveals dissociation-induced gene expression in tissue subpopulations. Nat Methods *14*, 935-936. 10.1038/nmeth.4437.